Frontiers in Bioscience Landmark

Front. Biosci. (Landmark Ed) **2026**; 31(11): 56498
https://doi.org/10.31083/FBL56498

Original Research

Systemic Mitochondrial Dysfunction in Mild and Severe Mouse Models of Duchenne Muscular Dystrophy: A Comparative Analysis of Skeletal Muscle, Heart, and Liver

Mikhail V. Dubinin[1], Anastasia E. Stepanova[1], Anastasia D. Igoshkina[1], Galina P. Drobot[1], Anna S. Ustinova[1], Alena A. Semenova[1], Irina B. Mikheeva[2], Ekaterina N. Kraeva[1], Svetlana O. Rakhmaeva[1], Tatiana V. Egorova[3], Konstantin N. Belosludtsev[4,5,6,*]

[1]Department of Biochemistry, Cell Biology and Microbiology, Mari State University, 424001 Yoshkar-Ola, Russia
[2]Laboratory of Experimental Neurobiology, Institute of Theoretical and Experimental Biophysics, Russian Academy of Sciences, 142290 Pushchino, Russia
[3]Laboratory of Modeling and Gene Therapy of Hereditary Diseases, Institute of Gene Biology, Russian Academy of Sciences, 119334 Moscow, Russia
[4]Laboratory of Mitochondrial Medicine, Institute of Theoretical and Experimental Biophysics, Russian Academy of Sciences, 142290 Pushchino, Russia
[5]Biophotonics Center, Prokhorov General Physics Institute, Russian Academy of Sciences, 119991 Moscow, Russia
[6]Department of Fundamental Sciences, Bauman Moscow State Technical University, 105005 Moscow, Russia
*Correspondence: bekonik@gmail.com (Konstantin N. Belosludtsev)

Academic Editor: Graham Pawelec
Submitted: 30 July 2026 Revised: 26 September 2026 Accepted: 30 September 2026 Published: 23 November 2026

Abstract

Background: Mitochondrial dysfunction is a key secondary pathogenic mechanism in Duchenne muscular dystrophy (DMD), yet its systemic nature across different tissues and its correlation with disease severity in mouse models remain poorly characterized. This study aimed to provide a comprehensive comparative analysis of mitochondrial dysfunction in skeletal muscle, heart, and liver between mild (*mdx*) and severe (D2.DMDdel8-34) mouse models of DMD. **Methods:** 8-week-old male mice from four strains were used: C57BL/10, *mdx*, DBA/2, and D2.DMDdel8-34. Mitochondrial oxidative phosphorylation (respiratory states 2, 3, 4 and respiratory control ratio), calcium retention capacity, and calcium overload were assessed in all three organs. Histopathological analyses (fibrosis, calcification, inflammation), ultrastructural examination, assessment of markers of oxidative stress (4-hydroxynonenal, 4-HNE) and calcium-dependent proteolysis (calpain activity), and functional tests (grip strength, wire hanging) were performed. **Results:** The D2.DMDdel8-34 model exhibited significantly more severe mitochondrial dysfunction across all three organs than the *mdx*. In skeletal muscle, D2.DMD showed a more pronounced decrease in respiratory function, accompanied by higher calcium overload and lower calcium retention capacity. Cardiac and hepatic mitochondria in D2.DMD also displayed reduced respiratory function. Calpain activity was markedly elevated only in the skeletal muscle of dystrophic mice, whereas cardiac and hepatic calpain activity remained unchanged. Oxidative stress markers were elevated in the skeletal muscle and heart of both dystrophic lines as well as in the liver of D2.DMD but not *mdx*. Ultrastructural analysis revealed severe myofibrillar disorganization and mitochondrial abnormalities in D2.DMD, with reduced mitochondrial number and size in skeletal muscle but evidence of compensatory mitochondrial proliferation in the heart. Stratified correlation analysis revealed pronounced differences between the genetic backgrounds: in the DBA/2-based group, strong associations were observed between mitochondrial dysfunction and tissue pathology in all three organs, whereas in the C57BL/10-based group, such associations were strong in skeletal muscle but limited in the heart and liver. **Conclusions:** The D2.DMDdel8-34 mouse model on the DBA/2 genetic background exhibits severe, systemic mitochondrial dysfunction across skeletal muscle, heart, and liver, supporting its utility as a model for investigating systemic mitochondrial pathology in DMD, although its limitations, including pronounced tissue calcification and impaired skeletal muscle regeneration, should be considered when interpreting these findings.

Keywords: Duchenne muscular dystrophy; mice; mitochondria; calcium; oxidative stress; calpain; skeletal muscle; heart; liver

1. Introduction

Duchenne muscular dystrophy (DMD) is a severe X-linked recessive disorder caused by mutations in the *DMD* gene, which encodes the dystrophin protein [1]. Dystrophin plays a critical role in maintaining the structural integrity of the sarcolemma by linking the cytoskeleton of the muscle fiber to the extracellular matrix through the dystrophin-associated protein complex [1]. Dystrophin deficiency leads to increased membrane fragility, uncontrolled entry of calcium ions (Ca^{2+}) from the extracellular space, and the initiation of a cascade of pathological events, including activation of calcium-dependent proteases (calpains), mitochondrial dysfunction, oxidative stress, myofiber necrosis, chronic inflammation, and fibrosis [1,2,3].

Copyright: © 2026 The Author(s). Published by IMR Press.
This is an open access article under the CC BY 4.0 license.

Publisher's Note: IMR Press stays neutral with regard to jurisdictional claims in published maps and institutional affiliations.

Although the underlying genetic defect in DMD is well understood, secondary pathophysiological mechanisms, such as mitochondrial dysfunction, which play a critical role in disease progression, require further elucidation [3]. Under conditions of chronic calcium overload, mitochondria lose their capacity for efficient adenosine triphosphate (ATP) synthesis, exhibit reduced resistance to the induction of the mitochondrial permeability transition pore (mPTP), and undergo morphological changes that ultimately contribute to cell death [3]. Importantly, when studied in preclinical models, the severity of both phenotypic manifestations and mitochondrial abnormalities can vary considerably and depends on the genetic background and the presence of modifier genes [4,5].

In preclinical research, the *mdx* mouse model on the C57BL/10ScSn genetic background is most widely used. However, these mice are characterized by a relatively mild disease course and high muscle regenerative capacity, which does not fully recapitulate the severe progressive pathology observed in patients [4,6]. To overcome this limitation, the D2.B10-*Dmdmdx*/J (D2-*mdx*) model was generated [4]. Recently, we obtained the D2.DMDdel8-34 line by transferring the DMD$^{del8\text{-}34}$ mutation onto the DBA/2 genetic background [7]. These mice exhibit a considerably more severe phenotype, including marked fibrosis, muscle calcification, reduced regeneration, and more profound metabolic disturbances, making them a more clinically relevant model for the progression of DMD in humans [4,5,6,7,8].

Previous studies have revealed substantial differences in the degree of mitochondrial dysfunction between the *mdx* and D2-*mdx* models. In particular, Tinklenberg and colleagues [8] demonstrated that D2-*mdx* mice exhibit a more pronounced reduction in mitochondrial respiration, virtually undetectable ATP levels, and significant ultrastructural damage in skeletal muscle compared with *mdx* mice. Similarly, we recently showed, using the severe D2.DMDdel8-34 model, a significantly greater decline in oxidative phosphorylation efficiency and resistance to mPTP induction than in *mdx* mice [7]. However, despite the overt multiorgan nature of DMD, a systematic analysis of mitochondrial dysfunction encompassing both contractile tissues (skeletal muscle and heart) and non-contractile organs (liver) in the context of comparing mild and severe phenotypes has not been performed to date. The inclusion of the liver in such an analysis is of particular interest, since the liver can be considered a control non-contractile organ that, according to published data, is not a primary target of systemic dysfunction in DMD [9]. This allows us to assess whether mitochondrial abnormalities are confined to contractile tissues or represent a more generalized phenomenon.

Thus, the aim of this study was to perform a comparative analysis of the degree of mitochondrial dysfunction in skeletal muscle, heart, and liver between mice with mild (*mdx*) and severe (D2.DMDdel8-34) DMD models. We assessed mitochondrial functional parameters (oxidative phosphorylation, calcium overload levels, and calcium retention capacity), markers of oxidative stress (4-hydroxynonenal, 4-HNE) and calcium-dependent proteolysis (calpain activity), conducted histological and ultrastructural analysis of affected tissues, as well as physiological tests. To gain deeper insight into the relationships between mitochondrial dysfunction and tissue pathology, we performed stratified correlation analysis separately for each genetic background (C57BL/10 + *mdx* and DBA/2 + D2.DMD), which allowed us to explore disease-related associations within each genetic background. We hypothesized that the D2.DMDdel8-34 model would exhibit more pronounced mitochondrial abnormalities in all organs examined (skeletal muscle, heart, and liver) compared with the *mdx* line, with the severity of these abnormalities correlating with the extent of histopathological phenotype. The findings will provide a rationale for using the D2.DMDdel8-34 line as a relevant model for investigating systemic mitochondrial pathology in DMD, while acknowledging that the model has specific features that distinguish it from the human disease.

2. Materials and Methods

2.1 Experimental Animals

Eight-week-old male mice of the following lines were used: C57BL/10ScSn (wild-type, hereafter C57BL/10), C57BL/10ScSn-Dmd*mdx* (hereafter *mdx*), DBA/2, and D2.DMDdel8-34 (hereafter D2.DMD). Animals of the C57BL/10 and DBA/2 lines were obtained from the Russian Academy of Sciences' Shemyakin and Ovchinnikov Institute of Bioorganic Chemistry ("Bio-model", Pushchino, Russia). D2.DMDdel8-34 mice were generated in the Laboratory of Modeling and Gene Therapy of Hereditary Diseases at the Institute of Gene Biology, Russian Academy of Sciences. All animals were housed under standard vivarium conditions with a 12-h light/dark cycle and had free access to water and food *ad libitum*. The animals received no pharmacological interventions.

2.2 Experimental Design

The study included four groups of animals, with 10 mice per group: C57BL/10, *mdx*, DBA/2, and D2.DMD. Animals were euthanized at 8 weeks of age by decapitation under isoflurane anesthesia (5% isoflurane, delivered via a TAIJI Small Animal Anesthesia Machine, RWD, Shenzhen, China). Whole blood was collected into tubes, allowed to clot at room temperature, and centrifuged at 800 ×*g* for 10 min at 4 °C. The resulting serum was aliquoted and stored at –80 °C. The quadriceps muscle (*vastus lateralis*), heart, and liver were immediately isolated for histological, electron microscopy, and biochemical analyses. Mitochondria were isolated from tissues immediately after sample collection.

2.3 Assessment of Muscle Strength and Endurance

Muscle strength was evaluated using a grip strength meter (IITC Life Science, Woodland Hills, CA, USA) according to a standard protocol. One week before the end of the experiment, animals were habituated to the testing procedure. Final measurements were performed one day before euthanasia. Results were expressed as grams of force per gram of body weight. The mean value from three consecutive trials was used for analysis.

Endurance was assessed using the wire-hanging test. The apparatus consisted of a 3-mm-diameter wire suspended 49 cm above a soft surface. The maximum holding time (in seconds) was recorded. To correct for the effect of body weight, the holding impulse was calculated as the product of holding time and body weight [10].

2.4 Analysis of Serum Creatine Kinase (CK) Activity

Total CK activity in serum was determined spectrophotometrically at 340 nm using a Multiskan GO plate reader (Thermo Fisher Scientific, Waltham, MA, USA) and commercial reagent kits (Vector-Best, Novosibirsk, Russia).

2.5 Histological Analysis

Samples of the quadriceps muscle, left ventricle of the heart, and liver were fixed in 10% neutral buffered formalin and embedded in paraffin using standard procedures. Serial sections of 5 µm thickness were obtained from each block using a Minux S710 rotary microtome (RWD, Shenzhen, China). Sections were stained with hematoxylin and eosin (H&E, Element Company, LLC, Saint Petersburg, Russia) for general morphology, with Sirius red (GC307014, Servicebio, Wuhan, China) for fibrosis detection, and with Alizarin red S (Interhim, LLC, Saint Petersburg, Russia) for detection of calcifications (the latter was omitted for liver).

Images were acquired using an EVOS M5000 microscope (Thermo Fisher Scientific, Waltham, MA, USA). Image analysis was performed blindly using ImageJ software (version 1.53, National Institutes of Health, Bethesda, MD, USA). In skeletal muscle, the proportion of centrally nucleated fibers (CNF) was determined. Fibrosis and calcification areas were quantified as the percentage of stained area relative to the total section area. Inflammatory foci were assessed on H&E-stained transverse sections, a focus was defined as a local accumulation of mononuclear cells (lymphocytes and macrophages) located within or immediately around muscle fibers and associated with fiber degeneration/necrosis, loss of cross-striation, and macrophage infiltration. Single scattered inflammatory cells were not counted. Fields of view were selected systematically (all fields) at ×40 magnification from the same anatomical region (mid-belly of the quadriceps muscle) in all animals. The number of inflammatory foci per field of view was recorded, the mean value per animal was used for between-group comparisons. In the heart, fibrosis area (Sirius red) and calcification area (Alizarin red S) were evaluated.

In the liver, on H&E-stained sections, the proportion of hepatocytes with ballooning degeneration (per 1000 cells) and the proportion of binucleated hepatocytes (per 1000 cells) were assessed as indicators of regenerative activity. The histological activity index (HAI, Knodell score) was calculated as the sum of scores for four components: periportal necrosis (0–10), intralobular necrosis (0–4), portal inflammation (0–4), and fibrosis (0–4) [11]. This scoring system was used because it allows a standardized, semi-quantitative assessment of key pathological features (periportal necrosis, intralobular necrosis, portal inflammation, and fibrosis) that are relevant to the hepatic changes observed in DMD. Although this scoring system was originally developed for chronic active hepatitis and has not been specifically validated for DMD models, it has been widely used in preclinical models of liver injury [11]. Additionally, the presence of Councilman bodies (apoptosis), hepatocyte mitoses, lymphohistiocytic infiltration, and signs of venous and sinusoidal congestion were recorded. Liver fibrosis was evaluated on Sirius red-stained sections as the percentage of red-stained area relative to the total section area.

2.6 Transmission Electron Microscopy (TEM)

Samples of the quadriceps muscle and left ventricle of the heart were fixed and processed according to a standard protocol [12]. Semithin sections (6 µm thick) were used to identify the mid-belly region and the transverse orientation of the fibers [13]. Ultrathin sections of 60–70 nm thickness were cut on a Leica EM UC6 ultramicrotome (Leica, Wetzlar, Germany), stained with uranyl acetate and lead citrate, and examined using a JEM-1400 transmission electron microscope (Jeol, Tokyo, Japan) at an accelerating voltage of 80 kV. Image analysis was performed using ImageJ 1.53c (National Institutes of Health, Bethesda, MD, USA). Mitochondrial morphometry was carried out by manual tracing of contours along the outer membrane. For each group, at least 150 mitochondrial profiles were analyzed (50 per sample). Area, number, perimeter, and shape of mitochondria, as well as cristae integrity and outer membrane integrity, were assessed. Sarcomere length was measured as the distance between two adjacent Z-disks along the longitudinal axis of the myofibril, and sarcomere width was measured perpendicular to the longitudinal axis at the level of the A-band. For each animal, measurements were performed in at least 10 randomly selected non-overlapping fields of view per section (at least 50 sarcomeres per animal), and the mean values were used for analysis. Mitophagosomes were identified as mitochondria enclosed within double-membrane autophagic vacuoles. Their number was counted in randomly selected fields and expressed per 50 μm^2 of section area. For each animal, at least 10 fields were analyzed. For statistical analysis, the mean values of all

morphometric parameters (mitochondrial and sarcomere) were first calculated for each animal, and these individual means ($n = 3$ per group) were used for comparisons between groups.

2.7 Isolation of Mitochondria

2.7.1 Isolation of Mitochondria From Skeletal Muscle

Mitochondria were isolated from the quadriceps muscles of both hind limbs by differential centrifugation [14]. After tissue collection, muscles were placed in ice-cold phosphate-buffered saline (PBS) (2.7 mM KCl, 1.5 mM KH_2PO_4, 136.9 mM NaCl, 8.9 mM Na_2HPO_4, 10 mM EDTA, pH 7.4) and washed free of blood. The tissue was minced with scissors, removing visible fat, ligaments, and connective tissue. The minced tissue was resuspended in 5 mL of ice-cold PBS buffer containing 10 mM EDTA and 0.05% trypsin and incubated on ice for 30 min. The suspension was centrifuged at 200 ×*g* for 5 min, and the supernatant was discarded. The pellet was homogenized in medium (67 mM sucrose, 50 mM KCl, 10 mM EDTA, 0.2% bovine serum albumin (BSA), 50 mM Tris-HCl, pH 7.4) using a rotor-stator homogenizer (Ultra-Turrax T 10 basic, IKA, Staufen, Germany) followed by transfer to a Potter-Elvehjem glass homogenizer (tissue-to-medium ratio 1:8). The homogenate was centrifuged at 700 ×*g* for 10 min, the supernatant was collected and centrifuged at 8000 ×*g* for 10 min. The pellet was resuspended in 5 mL of medium (250 mM sucrose, 10 mM Tris-HCl, pH 7.4) and re-centrifuged at 8000 ×*g* for 10 min. The final mitochondrial pellet was gently resuspended in a minimal volume of medium.

2.7.2 Isolation of Mitochondria From the Heart

The mitochondrial isolation protocol from the heart was similar to that described above, except for the trypsinization step. The rapidly excised heart was washed in PBS buffer, cut, and freed from remaining blood and connective tissue fragments. The organ was immediately transferred to homogenization medium (67 mM sucrose, 50 mM KCl, 10 mM EDTA, 0.2% BSA, 50 mM Tris-HCl, pH 7.4) and subjected to all further steps.

2.7.3 Isolation of Mitochondria From the Liver

The chilled liver was washed free of blood in isolation medium and minced with scissors into fragments of approximately 1 mm. Homogenization was performed manually using a Teflon pestle in a Potter-Elvehjem glass homogenizer in medium containing 250 mM sucrose, 1 mM EGTA, and 5 mM Hepes-KOH (pH 7.4) at a tissue-to-medium ratio of 1:10. The homogenate was centrifuged at 1200 ×*g* for 5 min. The supernatant was collected and centrifuged at 9800 ×*g* for 10 min. The resulting pellet was resuspended in 2 mL of isolation medium additionally containing BSA (2 mg/mL), then 15 mL of isolation medium without BSA was added, and the suspension was re-centrifuged at 9800 ×*g* for 10 min. The final mitochondrial pellet was resuspended in a small volume of isolation medium and kept on ice.

Mitochondrial protein concentration in all preparations was determined by the Bradford method using BSA as a standard.

2.8 Assessment of Mitochondrial Respiration and Oxidative Phosphorylation

Oxygen consumption rates of isolated mitochondria were recorded polarographically using a Clark-type electrode on an Oxygraph Plus system (Hansatech Instruments, King's Lynn, UK) at 25 °C. For skeletal muscle and heart mitochondria, the incubation medium contained 120 mM KCl, 5 mM NaH_2PO_4, 20 µM EGTA and 10 mM Hepes-KOH (pH 7.4). For liver mitochondria, the medium contained 200 mM sucrose, 20 mM KCl, 5 mM KH_2PO_4, 20 µM EGTA, 2 mM $MgCl_2$, and 10 mM Hepes-KOH (pH 7.4). Glutamate (2.5 mM) plus malate (2.5 mM) were used as oxidation substrates (complex I substrates). Respiration rates were measured in state 2 (in the presence of substrates without adenosine diphosphate, ADP), state 3 (after addition of 0.2 mM ADP), and state 4 (after ADP exhaustion). The respiratory control ratio (RCR) was calculated as the ratio of state 3 to state 4 respiration rates ($RCR = V_3/V_4$) [15]. The mitochondrial protein concentration in the chamber ranged from 0.2 to 0.5 mg/mL depending on the tissue. Respiration rates were expressed as nmol O_2/min per mg of mitochondrial protein.

2.9 Assessment of Mitochondrial Calcium Retention Capacity (CRC) and Calcium Overload

Mitochondrial CRC was assessed spectrophotometrically using the calcium-sensitive dye Arsenazo III (3,6-bis[(2-arsonophenyl)azo]-4,5-dihydroxy-2,7-naphthalenedisulfonic acid) [12]. Measurements were performed at 675–685 nm on Multiskan GO (Thermo Fisher Scientific, Waltham, MA, USA) plate reader at 25 °C. The absorbance intensity of the Ca^{2+}-Arsenazo III complex is proportional to the free calcium concentration in the medium. Mitochondria (0.2 mg protein/mL) were suspended in incubation medium containing 210 mM mannitol, 70 mM sucrose, 1 mM KH_2PO_4, 50 µM Arsenazo III, 10 µM EGTA, and 10 mM HEPES-KOH (pH 7.4). Glutamate (2.5 mM) plus malate (2.5 mM) were used as respiratory substrates. CRC was determined by sequential additions of $CaCl_2$ pulses (5 to 20 µM) to the mitochondrial suspension. The maximal amount of Ca^{2+} (nmol/mg protein) that mitochondria could accumulate before massive release occurred, indicating opening of the calcium-dependent mPTP, was recorded.

Mitochondrial calcium overload was assessed using the fluorescent dye Calcium Green-5N (C3737, Invitrogen, Carlsbad, CA, USA) and Varioskan LUX (Thermo Fisher Scientific, Waltham, MA, USA) plate reader. Mitochon-

dria (2 mg/mL) were incubated in medium containing 250 nM Calcium Green-5N. Addition of 40 µM alamethicin caused non-specific permeabilization of the membranes and release of calcium from the matrix, which was monitored by an increase in fluorescence [16]. Calcium overload was quantified as the area under the curve (AUC) of the fluorescence traces, reflecting the total amount of calcium released [7]. All reagents were from Sigma-Aldrich (St. Louis, MO, USA) unless otherwise stated.

2.10 Assessment of 4-HNE Levels in Tissues

The content of 4-HNE, a marker of oxidative stress, in homogenates of quadriceps muscle, heart, and liver was determined by enzyme-linked immunosorbent assay using a commercial kit (E-EL-0128, Elabscience, Wuhan, China) on a Multiskan GO plate reader (Thermo Fisher Scientific, Waltham, MA, USA). Results were normalized to total protein content.

2.11 Determination of Calpain Activity in Tissues

Calpain activity in tissue extracts of quadriceps muscle, heart, and liver was assessed using a commercial fluorometric kit (ab65308, Abcam, Cambridge, UK) according to the manufacturer's instructions. Samples were homogenized in extraction buffer that prevents calpain autoactivation. The fluorescence of the product generated by cleavage of the synthetic substrate Ac-LLY-AFC was measured after 60 min of incubation. Activity was expressed as relative fluorescence units (RFU) per mg of protein.

2.12 Statistical Analysis

Statistical analysis was performed using GraphPad Prism 10.4.0 (GraphPad Software, Boston, MA, USA). Data are presented as mean ± SEM. Normality was assessed by the Shapiro–Wilk test. Normally distributed parameters (respiratory and calcium homeostasis parameters, biochemical and functional tests, histomorphometric data except HAI) were analyzed by one-way analysis of variance (ANOVA) with Tukey's post-hoc test. Non-normally distributed parameters (HAI) were analyzed by Kruskal–Wallis test with Dunn's post-hoc test. HAI is presented as median (min–max). Correlation analysis was performed using Spearman's rank correlation coefficient (r_s), separately for each genetic background (C57BL/10-based and DBA/2-based groups). Within each genetic background, data from control and dystrophic animals were pooled to maximize statistical power and to assess the relationship between mitochondrial function and histopathology across the full range of phenotypic severity. The number of animals used for each correlation varied depending on the parameters analyzed (n = 8–10 per genetic background, corresponding to 4–5 control + 4–5 dystrophic animals). Correlation strength was interpreted as follows: $|r_s| > 0.7$—strong; $0.5 < |r_s| \leq 0.7$—moderate; $0.3 < |r_s| \leq 0.5$—weak; $|r_s| \leq 0.3$—negligible. Samples were allocated across assays based on tissue availability. All animals (n = 10 per group) were used for functional tests and serum CK activity. For histology, morphometry, and mitochondrial isolation, a subset of n = 5 animals per group was randomly selected from the main cohort. 4-HNE levels were measured in n = 4 per group, and calpain activity in n = 4–5 per group, depending on tissue availability. For TEM analysis, n = 3 animals per group were randomly selected from the n = 5 animals used for morphometry. No samples were excluded from the analysis. Sample size was not determined by formal power calculation; group sizes were chosen based on previous similar studies [7,12]. Correlation analyses were exploratory in nature and were performed without correction for multiple comparisons. Therefore, these results should be interpreted with caution. Exact p-values are provided for each correlation test. Differences were considered significant at $p < 0.05$.

3. Results

3.1 Model Validation and Characterization of Tissue Damage: Histopathological Changes and Stress Markers

To confirm the phenotypic differences between the *mdx* and D2.DMD lines and to validate the models used, we performed a comprehensive evaluation including functional tests, histopathological examination of skeletal muscle, heart, and liver, determination of serum creatine kinase levels, and assessment of oxidative stress (4-HNE) and calcium-dependent proteolysis (calpain) markers in tissues.

3.1.1 Functional Tests

Since young mice were used in the experiment, we expected to see minimal changes in muscle strength and endurance tests. Indeed, in *mdx* mice, grip strength was reduced 1.3-fold compared with C57BL/10 (Fig. 1A). At the same time, in D2.DMD mice, grip strength was decreased 2.0-fold compared with DBA/2, indicating a more pronounced reduction in muscle strength in the severe model relative to its respective control.

Endurance, evaluated by the holding impulse in the wire-hanging test, also differed between groups (Fig. 1B). In DBA/2 mice, this parameter was higher than in C57BL/10. In *mdx* mice, the holding impulse was reduced 4.3-fold compared with C57BL/10. In D2.DMD mice, the reduction was more pronounced – approximately 6.5-fold compared with DBA/2. Thus, both in grip strength and endurance, D2.DMD mice exhibited more profound impairments relative to their control (DBA/2) than *mdx* mice relative to C57BL/10.

3.1.2 Skeletal Muscle: Histopathological Changes, Creatine Kinase Levels, and Markers of Oxidative Stress and Calcium-Dependent Proteolysis

Histological analysis of the quadriceps muscle revealed characteristic dystrophinopathy-associated changes in both dystrophin-deficient lines. In *mdx* mice, focal areas

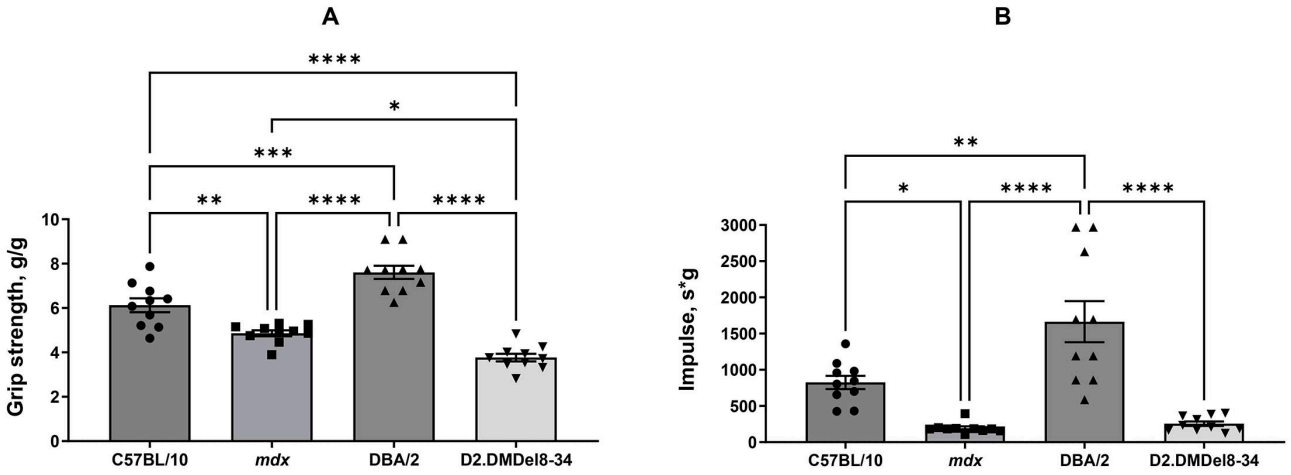

Fig. 1. Muscle strength and endurance in experimental mouse groups. (A) Grip strength normalized to body weight (g/g). (B) Holding impulse in the wire-hanging test (s × g). Data are presented as mean ± SEM (n = 10 per group). Each point represents an individual animal. Statistical significance was assessed by one-way ANOVA with Tukey's post-hoc test. *$p < 0.05$, **$p < 0.01$, ***$p < 0.001$, ****$p < 0.0001$.

of degeneration and regeneration of muscle fibers with centrally located nuclei (indicative of intense degeneration/regeneration cycles) and moderate inflammatory infiltration were observed. In D2.DMD mice, these changes were significantly more pronounced: extensive necrosis, marked disorganization of muscle tissue, multiple calcifications, intense fibrosis, and abundant inflammatory infiltration were noted (**Supplementary Figs. 1–3**).

Quantitative analysis showed that the proportion of centrally nucleated fibers was significantly lower in D2.DMD compared with *mdx* (Table 1). This reduction likely reflects the lower regenerative capacity of muscles on the DBA/2 genetic background, consistent with previously published data [17]. At the same time, the area of fibrosis and calcification and the number of inflammatory infiltrates were significantly higher in D2.DMD compared with *mdx*, confirming the more severe nature of the injury.

Serum CK activity was significantly elevated in both dystrophin-deficient lines compared with their respective controls (Table 1). In *mdx* mice, CK levels were approximately 2-fold higher than in C57BL/10, while in D2.DMD mice, they were approximately 2-fold higher than in DBA/2. Despite the more severe histological changes in D2.DMD, absolute CK values in this line were significantly lower than in *mdx*.

To assess oxidative stress in skeletal muscle, we measured 4-HNE content, a marker of lipid peroxidation (Table 1). 4-HNE levels were significantly elevated in *mdx* compared with C57BL/10. In D2.DMD mice, this parameter was significantly higher than in DBA/2 and also exceeded the level observed in *mdx*. Thus, oxidative stress in skeletal muscle was most pronounced in the severe D2.DMD model.

Calpain activity in skeletal muscle tissue, reflecting calcium-dependent proteolysis, was also elevated in both dystrophin-deficient lines (Table 1). In *mdx*, this parameter was significantly higher than in C57BL/10. In D2.DMD, calpain activity was significantly higher than in DBA/2 and also exceeded the level observed in *mdx*. Thus, activation of calcium-dependent proteolysis in skeletal muscle was also most pronounced in the severe D2.DMD model.

3.1.3 Heart: Histopathological Changes and Markers of Oxidative Stress and Calcium-Dependent Proteolysis

Histological examination of the left ventricle revealed fibrotic changes in both dystrophin-deficient lines (**Supplementary Fig. 4**). Sirius red staining showed that the fibrosis area was significantly higher in D2.DMD compared with DBA/2 and *mdx*, while no significant differences were observed between C57BL/10 and *mdx* (Table 1). Alizarin red staining revealed calcification foci in the myocardium (**Supplementary Fig. 5**), which were significantly more pronounced in D2.DMD compared with DBA/2 and *mdx*, whereas in *mdx* only a trend toward elevation relative to C57BL/10 was noted (Table 1). As previously reported, cardiac pathology in *mdx* mice on the C57BL/10 background is typically mild or absent at 8 weeks of age and develops only later [4,5]. By contrast, the DBA/2 genetic background markedly accelerates cardiac involvement, resulting in significant fibrosis and calcification in D2.DMD as early as 8 weeks, consistent with the more aggressive cardiac phenotype described in D2-*mdx* mice [4,5].

4-HNE levels in cardiac tissue, like calpain activity, were significantly lower than in skeletal muscle (Table 1), reflecting tissue-specific differences in the intensity of oxidative stress and calcium-dependent proteolysis. Notably, 4-HNE levels were significantly elevated in *mdx* compared with C57BL/10 and in D2.DMD compared with DBA/2,

Table 1. Histopathological parameters, markers of oxidative stress and calcium-dependent proteolysis in skeletal muscle, heart, and liver of experimental mouse groups.

Parameter	C57BL/10	*mdx*	DBA/2	D2.DMD
Skeletal muscle				
CK, U/L (n = 10)	531.96 ± 41.55	1059.28 ± 46.93*	396.09 ± 28.72	755.08 ± 97.41$^{\#¥}$
CNF, % (n = 5)	0.93 ± 0.23	43.44 ± 3.75*	0.78 ± 0.22	18.54 ± 2.55*$^{\#¥}$
Inflammatory foci, per field (n = 5)	0.00 ± 0.00	1.37 ± 0.19*	0.00 ± 0.00	24.05 ± 2.77*$^{\#¥}$
Fibrosis area, % (n = 5)	0.50 ± 0.11	7.43 ± 0.81*	0.65 ± 0.16	23.42 ± 1.29*$^{\#¥}$
Calcification area, % (n = 5)	0.004 ± 0.001	0.031 ± 0.004	0.004 ± 0.001	7.537 ± 1.092*$^{\#¥}$
4-HNE, pmol/mg protein (n = 4)	7.66 ± 0.46	13.13 ± 0.77*	10.62 ± 1.13	17.32 ± 0.86*$^{\#¥}$
Calpain activity, RFU/mg protein (n = 5)	33.94 ± 2.87	100.56 ± 13.98*	37.54 ± 2.98	269.79 ± 20.94*$^{\#¥}$
Heart				
Fibrosis area, % (n = 5)	0.33 ± 0.07	0.84 ± 0.11	0.52 ± 0.22	3.03 ± 0.88*$^{\#¥}$
Calcification area, % (n = 5)	0.0003 ± 0.0003	0.0899 ± 0.0351	0.0002 ± 0.0002	0.2893 ± 0.0417*$^{\#¥}$
4-HNE, pmol/mg protein (n = 4)	2.54 ± 0.05	3.45 ± 0.14*	2.50 ± 0.08	3.30 ± 0.10*$^{\#}$
Calpain activity, RFU/mg protein (n = 5)	14.92 ± 0.85	17.00 ± 0.77	10.54 ± 0.48*$^{¥}$	11.42 ± 0.60*$^{¥}$
Liver				
Ballooning degeneration, ‰ (n = 5)	6.59 ± 1.81	380.22 ± 101.55*	71.90 ± 26.50*	445.80 ± 86.32*$^{\#}$
Binucleated hepatocytes, ‰ (n = 5)	87.14 ± 7.84	163.98 ± 7.23*	190.51 ± 4.84*	163.92 ± 8.29*
Fibrosis area, % (n = 5)	0.003 ± 0.001	0.015 ± 0.005	0.051 ± 0.010	0.119 ± 0.027*$^{\#¥}$
HAI (n = 5)	1.00 (1.00–4.00)	5.00 (4.75–5.00)*	4.50 (4.00–5.00)*	5.50 (4.00–7.00)*
4-HNE, pmol/mg protein (n = 4)	1.66 ± 0.08	1.56 ± 0.14	1.45 ± 0.10	1.98 ± 0.11$^{\#}$
Calpain activity, RFU/mg protein (n = 4)	60.48 ± 3.76	63.29 ± 4.01	44.46 ± 0.97*$^{¥}$	52.27 ± 2.62

Data are expressed as mean ± SEM, except for HAI, which is presented as median (min–max). *$p < 0.01$ vs C57BL/10; $^{\#}p < 0.01$ vs DBA/2; $^{¥}p < 0.01$ vs *mdx*. CK, creatine kinase; CNF, centrally nucleated fibers; 4-HNE, 4-hydroxynonenal; RFU, relative fluorescence units; HAI, histological activity index.

while no significant differences were observed between *mdx* and D2.DMD, or between C57BL/10 and DBA/2 (Table 1).

Calpain activity in cardiac tissue was determined exclusively by the genetic background: in DBA/2 and D2.DMD mice, this parameter was significantly lower than in C57BL/10 and *mdx*, while dystrophin-deficient mice did not differ from their respective controls within each genetic line (Table 1).

3.1.4 Liver: Histopathological Changes and Markers of Oxidative Stress and Calcium-Dependent Proteolysis

Histological analysis of the liver revealed pathological changes in all groups of dystrophin-deficient mice (**Supplementary Figs. 6,7**, Table 1). In C57BL/10 mice, only isolated foci of dystrophy and rare focal necrosis were noted, with a minimal histological activity index.

In the liver of *mdx* mice, along with foci of dystrophy, areas of hepatocyte disorganization, ductular proliferation, increased numbers of binucleated cells, and microgranulomas were observed, reflecting activation of inflammatory and regenerative responses.

In DBA/2 animals, by contrast, fine-vacuolar dystrophy predominated, with marked intracellular cholestasis and sinusoidal congestion, at a level of inflammatory changes similar to that in *mdx*.

The most severe changes were found in D2.DMD mice. Although the HAI score in D2.DMD was not different from that in DBA/2, the pattern of hepatic injury was qualitatively distinct and more severe. Ballooning degeneration of hepatocytes, characterized by cell swelling and cytoplasmic clearing, was significantly more pronounced in *mdx* and D2.DMD compared with control groups, with no significant differences between the two dystrophin-deficient lines (Table 1). However, in D2.DMD, additional features were observed: diffusely distributed Councilman bodies (apoptosis marker), hepatocyte mitoses, lymphohistiocytic infiltration in areas of necrosis, and the most pronounced venous and sinusoidal congestion (**Supplementary Fig. 6**). The number of binucleated hepatocytes, reflecting regenerative activity, was significantly increased in DBA/2, *mdx*, and D2.DMD compared with C57BL/10, with no differences among these groups (Table 1).

Sirius red staining revealed fibrotic changes in the liver (**Supplementary Fig. 7**). The fibrosis area was significantly higher in D2.DMD compared with DBA/2 and *mdx*, while no significant differences were found between C57BL/10 and *mdx* (Table 1). In C57BL/10 and *mdx* mice, fibrosis was minimal or absent, whereas in D2.DMD distinct periportal and perisinusoidal fibrosis was observed.

4-HNE levels in liver tissue were significantly elevated only in D2.DMD compared with DBA/2, while no

differences were observed among the other groups (Table 1). Calpain activity in the liver was significantly lower in DBA/2 compared with both C57BL/10 and *mdx*, while D2.DMD did not differ from *mdx*. Dystrophin-deficient mice did not differ from their respective controls within each genetic line (Table 1).

Thus, the histological picture of the liver confirms the systemic nature of DMD pathology, with the most severe changes in the D2.DMD line, including pronounced ballooning degeneration, apoptosis, inflammatory infiltration, congestion, activation of regenerative processes, and fibrosis.

3.2 Mitochondrial Dysfunction in Skeletal Muscle, Heart, and Liver

Since histopathological analysis revealed the most severe changes in the D2.DMD line across all three organs, we assessed the functional state of mitochondria in skeletal muscle, heart, and liver. For each tissue, we determined the efficiency of oxidative phosphorylation, mitochondrial CRC, which reflects resistance to mPTP induction, and the level of mitochondrial calcium overload.

3.2.1 Skeletal Muscle

Mitochondria isolated from the quadriceps muscle demonstrated significant differences in respiratory parameters between groups (**Supplementary Fig. 8**, Table 2). State 2 respiration (basal respiration in the presence of substrates without ADP) was lower in DBA/2 and D2.DMD mice compared with C57BL/10 and *mdx*. State 3 respiration (phosphorylating respiration stimulated by ADP addition) was reduced in DBA/2 compared with C57BL/10, in *mdx* compared with C57BL/10, and was lowest in D2.DMD, which differed significantly from all other groups. State 4 respiration (respiration after ADP exhaustion) was lower in DBA/2 and D2.DMD mice compared with C57BL/10 and *mdx*, with no differences between DBA/2 and D2.DMD or between C57BL/10 and *mdx*. The RCR, reflecting the efficiency of coupling between respiration and oxidative phosphorylation, was decreased in *mdx* compared with C57BL/10, whereas DBA/2 did not differ from C57BL/10. D2.DMD exhibited the lowest RCR among all groups, significantly lower than in DBA/2, *mdx*, and C57BL/10.

Assessment of mitochondrial calcium homeostasis revealed a direct relationship between two key parameters—calcium overload and CRC (Fig. 2). In D2.DMD mitochondria, calcium overload was significantly higher compared with *mdx* and controls, reflecting excessive Ca^{2+} accumulation in the matrix (Fig. 2A,C). In *mdx*, this parameter was also elevated compared with C57BL/10, albeit to a lesser extent than in D2.DMD. A consequence of this was a reduction in CRC parameters—the ability of mitochondria to retain additional Ca^{2+} without opening the mPTP [18]. Mitochondrial CRC in *mdx* was significantly lower than in C57BL/10 (Fig. 2B,D). In the DBA/2 line, this parameter was also decreased compared with C57BL/10 and did not differ from *mdx*, indicating background features of mitochondrial calcium homeostasis characteristic of the DBA/2 genetic background. The most pronounced reduction in CRC was observed in D2.DMD: this parameter was significantly lower than in DBA/2, *mdx*, and C57BL/10. Moreover, the extent of this reduction in D2.DMD relative to DBA/2 exceeded that in *mdx* relative to C57BL/10. Thus, increased mitochondrial calcium overload in D2.DMD directly underlies the reduction in their CRC, creating a predisposition for premature mPTP opening and initiation of cell death.

Collectively, these data indicate that mitochondrial dysfunction in skeletal muscle is significantly more pronounced in the severe D2.DMD model, manifesting as impaired coupling of oxidative phosphorylation and disruption of calcium homeostasis.

3.2.2 Heart

Mitochondria isolated from the heart exhibited different patterns of respiratory changes compared with skeletal muscle (**Supplementary Fig. 9**, Table 2). State 2 respiration did not differ among groups, indicating comparable basal electron transport chain activity in the absence of a phosphorylating substrate. State 3 respiration was significantly higher in *mdx* mice compared with C57BL/10. In the DBA/2 line, this parameter was 1.8-fold higher than in C57BL/10 and 1.5-fold higher than in *mdx*, reflecting higher cardiac mitochondrial respiratory activity in this genetic line. In D2.DMD, by contrast, a significant decrease in state 3 respiration was observed compared with DBA/2, although it remained significantly higher than in C57BL/10 and *mdx*. State 4 respiration was significantly higher in DBA/2 compared with C57BL/10, while dystrophin-deficient mice (both *mdx* and D2.DMD) did not differ from their respective controls within each genetic line. The RCR was significantly elevated in DBA/2 compared with both C57BL/10 and *mdx*, reflecting higher coupling efficiency in this line. RCR was significantly higher in *mdx* compared with C57BL/10. In D2.DMD, by contrast, RCR was significantly decreased compared with DBA/2, although it remained significantly higher than in C57BL/10 and *mdx*.

Analysis of mitochondrial calcium homeostasis in the heart revealed differences from skeletal muscle (Fig. 3). Mitochondrial calcium overload was increased only in D2.DMD compared with DBA/2, while no differences were observed among the other groups (Fig. 3A,C). Notably, the increase in calcium overload in the heart was significantly less pronounced than in skeletal muscle. Mitochondrial CRC did not differ between C57BL/10 and DBA/2 (Fig. 3B,D). In *mdx*, this parameter was significantly higher than in C57BL/10 and DBA/2. In D2.DMD, by contrast, CRC was significantly decreased compared with DBA/2 and *mdx*.

Table 2. Respiratory parameters of mitochondria from skeletal muscle, heart, and liver of experimental mouse groups.

Parameter	C57BL/10	*mdx*	DBA/2	D2.DMD
Skeletal muscle (n = 5)				
State 2	33.0 ± 0.2	31.2 ± 0.2	27.9 ± 0.3*¥	27.5 ± 0.6*¥
State 3	201.0 ± 1.9	160.9 ± 2.6*	148.2 ± 3.9*	99.6 ± 6.5*#¥
State 4	45.0 ± 1.5	47.0 ± 1.2	33.6 ± 1.1*¥	37.3 ± 0.9*¥
RCR	4.5 ± 0.2	3.4 ± 0.1*	4.4 ± 0.1¥	2.7 ± 0.2*#¥
Heart (n = 5)				
State 2	20.2 ± 0.5	19.4 ± 0.5	21.0 ± 0.7	21.9 ± 2.0
State 3	50.3 ± 1.0	58.2 ± 1.3*	88.7 ± 2.6*¥	68.2 ± 3.9*#¥
State 4	22.1 ± 0.4	22.3 ± 0.7	26.5 ± 0.8*¥	23.8 ± 1.6
RCR	2.3 ± 0.1	2.6 ± 0.1*	3.4 ± 0.2*¥	2.9 ± 0.1*#¥
Liver (n = 5)				
State 2	12.8 ± 0.4	11.4 ± 0.7	12.2 ± 0.7	11.6 ± 0.5
State 3	50.2 ± 1.1	51.7 ± 1.1	60.9 ± 1.7*¥	49.9 ± 2.1#
State 4	16.3 ± 0.5	15.5 ± 0.7	14.2 ± 0.4	16.3 ± 0.8
RCR	3.1 ± 0.1	3.4 ± 0.1	4.3 ± 0.2*¥	3.1 ± 0.2#

Respiration rates (State 2, State 3, and State 4) are expressed as nmol O_2/min per mg of mitochondrial protein. RCR is expressed as relative units (ratio of State 3 to State 4 respiration). State 3 mitochondrial respiration was initiated by the addition of 200 µM ADP. Data are expressed as mean ± SEM (n = 5). *$p < 0.01$ vs C57BL/10; #$p < 0.01$ vs DBA/2; ¥$p < 0.01$ vs *mdx*. RCR, respiratory control ratio; ADP, adenosine diphosphate.

Thus, despite minimal histopathological changes at 8 weeks of age, distinct mitochondrial dysfunction was already detectable in both dystrophic lines. However, the direction of alterations differed: *mdx* showed a tendency toward enhanced respiratory function and increased CRC, suggesting a compensatory response, whereas D2.DMD exhibited suppressed oxidative phosphorylation and reduced CRC, indicating early pathological decompensation. These findings indicate that mitochondrial abnormalities are already detectable at 8 weeks of age, including in tissues with relatively limited histopathology, but they do not establish the temporal sequence of these changes.

3.2.3 Liver

In liver mitochondria, respiratory dysfunction was observed, the pattern of which differed from that in skeletal muscle and heart (**Supplementary Fig. 10**, Table 2). State 2 respiration did not differ among groups. State 3 respiration in *mdx* did not differ from C57BL/10. In the DBA/2 line, this parameter was 1.2-fold higher than in C57BL/10 and *mdx*, reflecting higher hepatic mitochondrial respiratory activity in this genetic line. In D2.DMD, by contrast, a significant decrease in state 3 respiration was observed compared with DBA/2, to a level comparable to that in *mdx* and C57BL/10. State 4 respiration did not differ among groups. The RCR was highest in DBA/2 (1.4-fold above C57BL/10 and D2.DMD, 1.3-fold above *mdx*), while D2.DMD returned to the level of C57BL/10 and *mdx*.

Analysis of mitochondrial calcium homeostasis in the liver revealed alterations whose pattern also differed from that in skeletal muscle (Fig. 4). Mitochondrial calcium overload was increased only in D2.DMD compared with all other groups, while no differences were observed among C57BL/10, *mdx*, and DBA/2 (Fig. 4A,C). Notably, the increase in calcium overload in the liver was significantly less pronounced than in skeletal muscle. CRC was comparable between C57BL/10 and *mdx*, and between C57BL/10 and DBA/2, but was significantly higher in DBA/2 compared with *mdx* and D2.DMD (Fig. 4B,D).

3.3 Ultrastructural Changes in Skeletal Muscle and Heart

Ultrastructural analysis was performed on skeletal muscle and heart, as these contractile tissues exhibit well-defined structural features (sarcomeres, Z-disks, myofibrillar organization) that are directly linked to their mechanical function and are critically affected in dystrophin deficiency. For the liver, the key pathological alterations (ballooning degeneration, inflammation, and fibrosis) were reliably assessed by histological analysis (Section 3.1.4), and therefore transmission electron microscopy was not performed for this tissue.

3.3.1 Skeletal Muscle

Electron microscopy analysis of skeletal muscle revealed progressive ultrastructural changes in dystrophin-deficient mice, most pronounced in the D2.DMD line (**Supplementary Fig. 11**, Table 3).

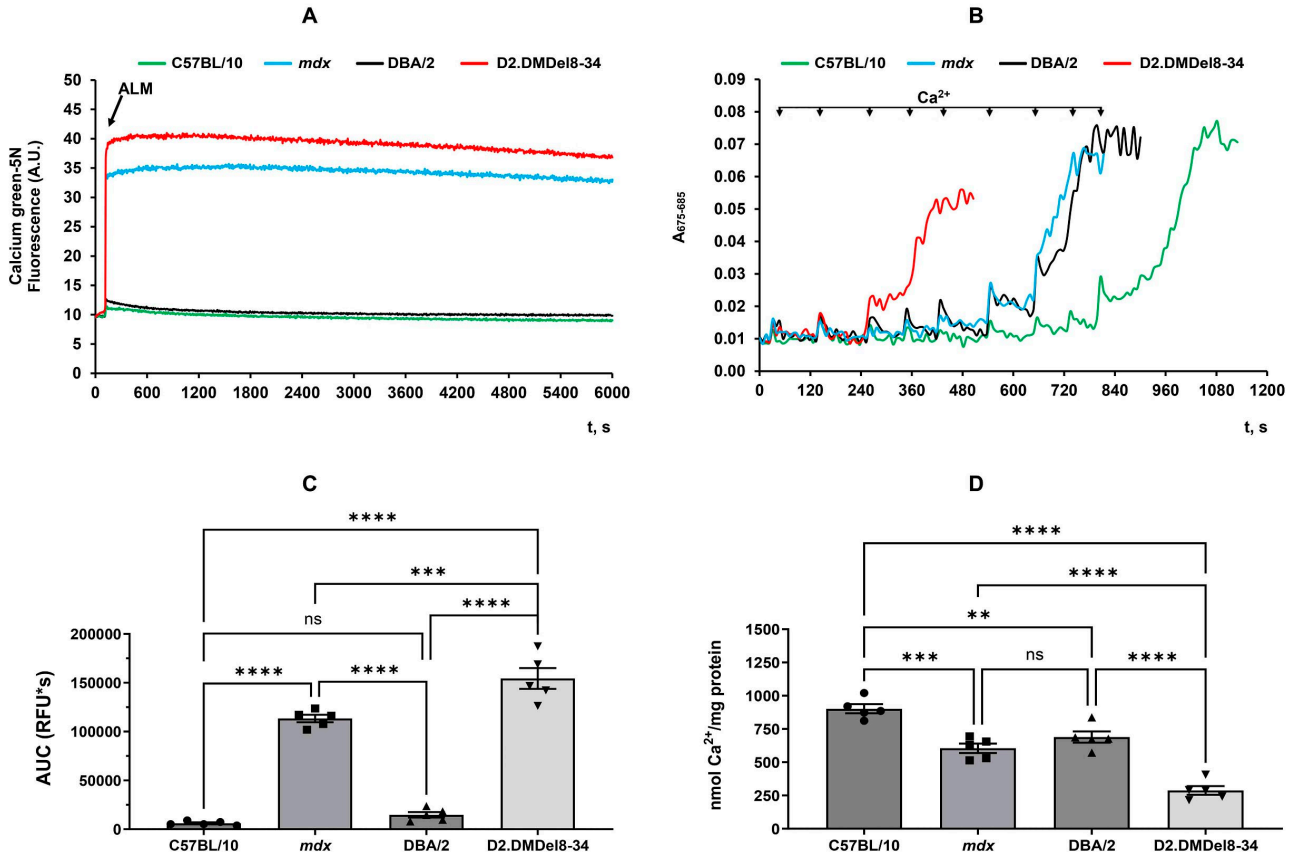

Fig. 2. Mitochondrial calcium homeostasis in skeletal muscle mitochondria. (A) Representative traces of Calcium Green-5N fluorescence intensity in mitochondria isolated from quadriceps muscles of the experimental mouse groups. Alamethicin (ALM, 40 µM) was added at the time indicated by the arrow to induce maximal calcium release from the mitochondrial matrix. (B) Representative traces of external Ca^{2+} concentration changes following sequential additions of 20 µM $CaCl_2$ pulses to mitochondrial suspensions. (C) Quantification of total calcium release presented as the area under the curve (AUC) of the fluorescence traces. Data are expressed as mean ± SEM. Mitochondria (2 mg/mL) were incubated with glutamate and malate as substrates. (D) Quantitative analysis of calcium retention capacity (CRC) of isolated quadriceps mitochondria. Data are expressed as mean ± SEM. Mitochondria (0.2 mg/mL) were incubated with glutamate and malate as substrates. The traces shown in (A,B) are from representative experiments conducted on single mitochondrial samples, similar results were obtained in four additional independent experiments. $^{**}p < 0.01$, $^{***}p < 0.001$, $^{****}p < 0.0001$; ns, not significant.

Table 3. Morphometric parameters of skeletal muscle and cardiac ultrastructure from experimental mouse groups.

Parameter	C57BL/10	*mdx*	DBA/2	D2.DMD
Skeletal muscle ($n = 3$)				
Sarcomere length, µm	1.95 ± 0.05	2.02 ± 0.06	1.80 ± 0.04*	1.84 ± 0.03
Sarcomere width, µm	0.96 ± 0.02	0.58 ± 0.02*	0.71 ± 0.02*	0.80 ± 0.05*¥
Mitochondrial number, N/25 µm^2	13.73 ± 0.93	13.36 ± 1.17	25.35 ± 1.45*¥	8.55 ± 1.05#
Mitochondrial perimeter, µm	2.87 ± 0.02	1.90 ± 0.07*	2.76 ± 0.11¥	1.22 ± 0.10*#¥
Mitophagosomes, N/50 µm^2	0.27 ± 0.09	1.12 ± 0.14*	0.67 ± 0.10	1.57 ± 0.20*#
Heart ($n = 3$)				
Mitochondrial number, N/25 µm^2	17.21 ± 1.39	20.89 ± 1.02	22.92 ± 0.62*	24.44 ± 0.99*
Mitochondrial perimeter, µm	3.78 ± 0.19	3.19 ± 0.13	3.24 ± 0.23	3.15 ± 0.19
Mitophagosomes, N/50 µm^2	0.69 ± 0.33	2.27 ± 0.35*	2.67 ± 0.36*	5.08 ± 0.12*#¥

Data are expressed as mean ± SEM. *$p < 0.01$ vs C57BL/10; #$p < 0.01$ vs DBA/2; ¥$p < 0.01$ vs *mdx*.

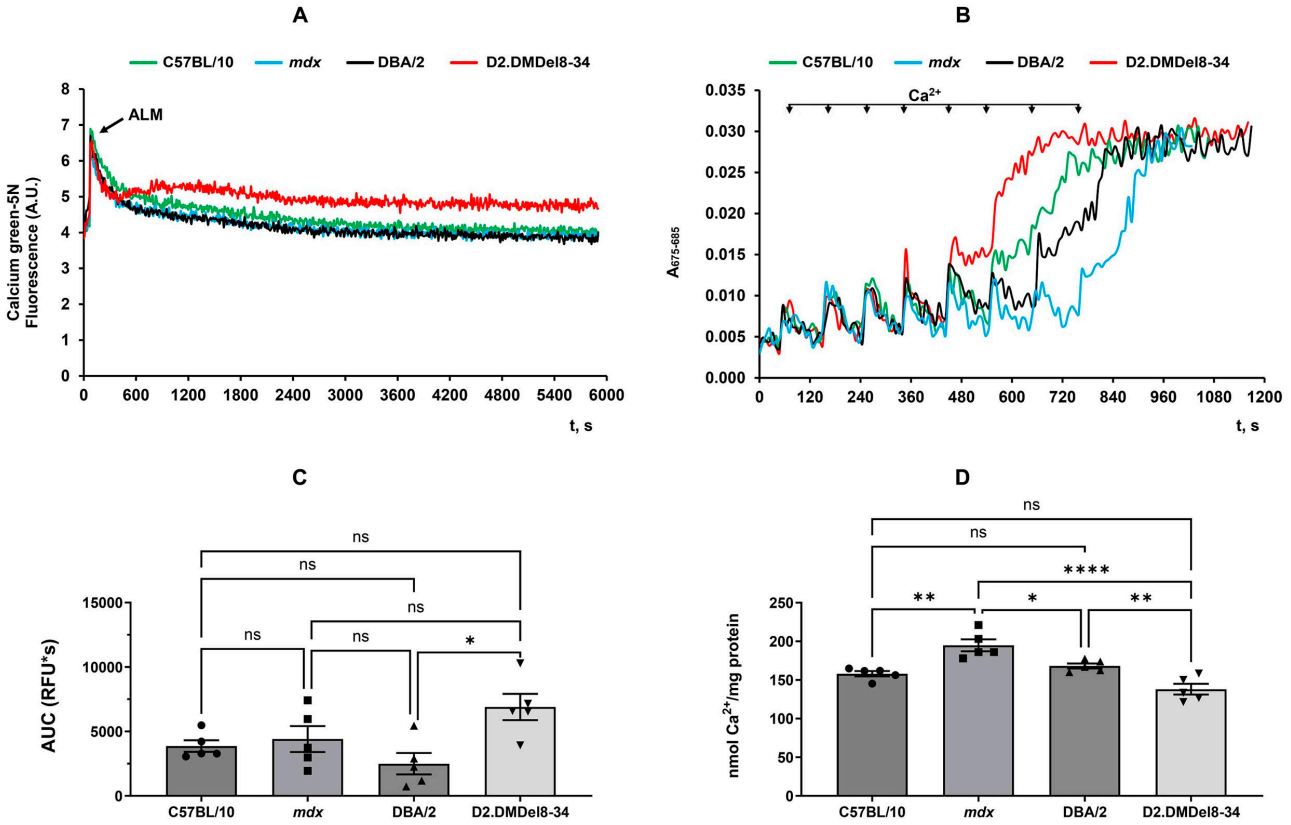

Fig. 3. Mitochondrial calcium homeostasis in cardiac mitochondria. (A) Representative traces of Calcium Green-5N fluorescence intensity in mitochondria isolated from the hearts of the experimental mouse groups. Alamethicin (ALM, 40 µM) was added at the time indicated by the arrow to induce maximal calcium release from the mitochondrial matrix. (B) Representative traces of external Ca^{2+} concentration changes following sequential additions of 5 µM $CaCl_2$ pulses to mitochondrial suspensions. (C) Quantification of total calcium release presented as the area under the curve (AUC) of the fluorescence traces. Data are expressed as mean ± SEM. Mitochondria (2 mg/mL) were incubated with glutamate and malate as substrates. (D) Quantitative analysis of CRC of isolated cardiac mitochondria. Data are expressed as mean ± SEM. Mitochondria (0.2 mg/mL) were incubated with glutamate and malate as substrates. The traces shown in (A,B) are from representative experiments conducted on single mitochondrial samples, similar results were obtained in four additional independent experiments. *$p < 0.05$, **$p < 0.01$, ****$p < 0.0001$; ns, not significant.

In C57BL/10 mice, typical sarcomere organization with clear transverse striation, well-defined M- and Z-disks, and parallel alignment of myofilaments was observed. Mitochondria in the subsarcolemmal zone were present as sparse clusters of spherical organelles without signs of cristae destruction. Interfibrillar mitochondria had an oval or elongated shape and were arranged linearly, oriented parallel to myofibrils. The sarcoplasmic reticulum was represented predominantly by small flattened cisternae.

In *mdx* mice, mosaic degenerative changes of focal character were observed, coexisting with preserved areas of fibers. Myocyte nuclei were most often centrally located. Thinning of myofibrils was noted while overall sarcomeric organization was preserved, however, Z-lines were often angled relative to the longitudinal axis of the fiber or had a wavy appearance, and occasionally their ruptures were observed. Sarcomere width was significantly reduced compared with C57BL/10, while sarcomere length did not differ between *mdx* and C57BL/10 (Table 3). Interfibrillar spaces were expanded due to increased sarcoplasmic volume, with elevated glycogen and secondary lysosome content. The sarcoplasmic reticulum was significantly dilated, and its cisternae proliferated and formed vesicles surrounding mitochondria. Mitochondrial number in *mdx* muscles did not differ from C57BL/10, but their perimeter (size) was significantly reduced (Table 3). An increase in the number of mitophagosomes was noted compared with C57BL/10.

In DBA/2 mice, moderate structural changes were observed: thinning and disorganization of myofilaments with preservation of overall sarcomeric architecture, blurred and deformed Z-disks, and dilation of sarcoplasmic reticulum cisternae. Sarcomere length was significantly reduced in DBA/2 compared with C57BL/10, and sarcomere width was also significantly smaller than in C57BL/10, but did not differ from *mdx* or D2.DMD (Table 3). The number of mitochondria in DBA/2 was approximately twice as high as

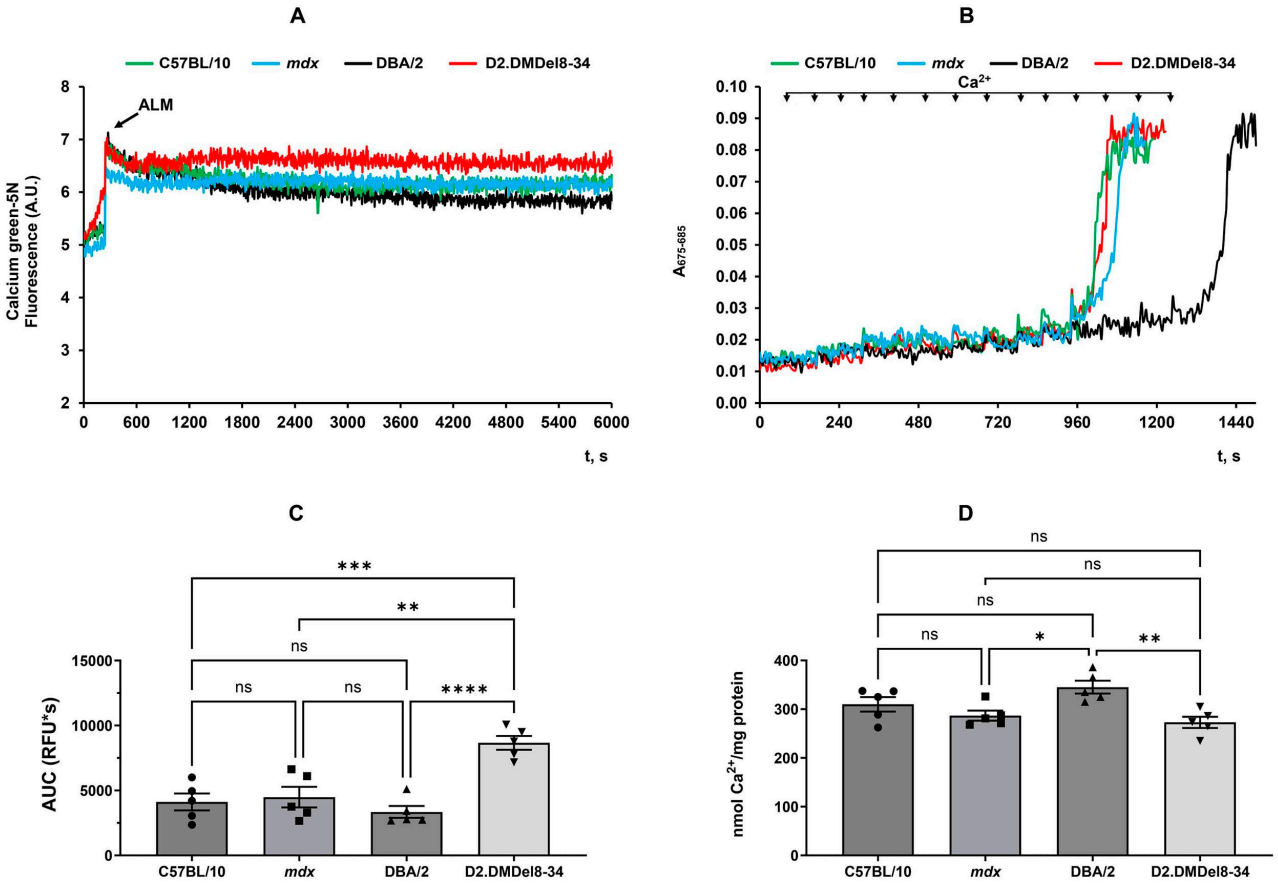

Fig. 4. Mitochondrial calcium homeostasis in liver mitochondria. (A) Representative traces of Calcium Green-5N fluorescence intensity in mitochondria isolated from the livers of the experimental mouse groups. Alamethicin (ALM, 40 µM) was added at the time indicated by the arrow to induce maximal calcium release from the mitochondrial matrix. (B) Representative traces of external Ca^{2+} concentration changes following sequential additions of 5 µM $CaCl_2$ pulses to mitochondrial suspensions. (C) Quantification of total calcium release presented as the area under the curve (AUC) of the fluorescence traces. Data are expressed as mean ± SEM. Mitochondria (2 mg/mL) were incubated with glutamate and malate as substrates. (D) Quantitative analysis of CRC of isolated liver mitochondria. Data are expressed as mean ± SEM. Mitochondria (0.2 mg/mL) were incubated with glutamate and malate as substrates. The traces shown in (A,B) are from representative experiments conducted on single mitochondrial samples, similar results were obtained in four additional independent experiments. *$p < 0.05$, **$p < 0.01$, ***$p < 0.001$, ****$p < 0.0001$; ns, not significant.

in C57BL/10 and *mdx*. Their perimeter did not differ from C57BL/10 but was significantly larger than in *mdx*. In the subsarcolemmal zone, mitochondria formed large clusters, represented by both normal spherical and giant polymorphic forms.

The most severe changes were found in D2.DMD mice. Pronounced disturbances of the contractile apparatus were observed: thinning of myofibrils, disorganization of myofilaments, and altered orientation of Z-lines with areas of rupture. In severe cases, foci of complete degeneration with myolysis were noted. Interfibrillar spaces were significantly expanded due to increased sarcoplasmic volume. The sarcoplasmic reticulum exhibited marked dilation and enhanced branching. A characteristic feature was deep structural changes of the sarcolemma with formation of numerous alternating invaginations and protrusions. The number of mitochondria in the D2.DMD group was nearly 3-fold lower than in DBA/2, and their perimeter was significantly smaller than in DBA/2, *mdx*, and C57BL/10. The number of mitophagosomes in the D2.DMD group was the highest among all groups; however, no significant differences from *mdx* were observed. Sarcomere width in D2.DMD was significantly smaller than in C57BL/10 and significantly larger than in *mdx*, but did not differ from DBA/2.

3.3.2 Heart

Electron microscopic analysis of cardiomyocytes revealed ultrastructural changes whose pattern differed from that in skeletal muscle (**Supplementary Fig. 12**, Table 3).

In C57BL/10 mice, the contractile apparatus was represented by ordered myofibrils with clearly distinguishable

sarcomeres, Z-disks, and correctly oriented filaments. Mitochondria exhibited preserved ultrastructure with dense matrix, distinct parallel cristae, and uniform distribution between myofibrils.

In the *mdx* group, disorganization of the contractile apparatus with disruption of sarcomere structure, pyknosis of nuclei, and pronounced mitochondrial polymorphism, from severely swollen forms with fragmented cristae to organelles with hypercondensed matrix, were noted. Significant hypertrophy of the sarcoplasmic reticulum and increased numbers of lipid inclusions were observed. Mitochondrial number and perimeter in the *mdx* heart did not differ from C57BL/10 (Table 3). However, the number of mitophagosomes in *mdx* was significantly higher than in C57BL/10.

In both DBA/2 and D2.DMD groups, significant destructive changes in cardiomyocytes were observed. The most pronounced disturbances were noted in the structure and organization of myofibrils, indicative of profound disorganization of the contractile apparatus. Myofibrils were thinned, with a loose structure and chaotic arrangement. Fragmentation of Z-disks with loss of transverse striation and foci of myofilament lysis were noted. Sarcoplasmic reticulum cavities were markedly dilated.

Mitochondria lost their ordered arrangement along myofibrils and formed scattered clusters of varying sizes. They exhibited pronounced polymorphism in size and shape, disruption of cristae structure (fragmentation, rarefaction, chaotic arrangement), and local areas of matrix clearing. Of particular note was the abundance of pathological mitochondrial forms: megamitochondria significantly exceeding normal size, septated mitochondria with internal septa, and mitochondria with micromitophagosomes. Mitochondrial number in the DBA/2 and D2.DMD hearts was significantly higher than in C57BL/10 but did not differ from *mdx*. Mitochondrial perimeter did not differ among the groups (Table 3). The only parameter that differed significantly between D2.DMD and its background was the number of mitophagosomes. Their number was the highest among all groups and significantly exceeded the levels observed in DBA/2 and *mdx*.

3.4 Correlation Analysis

To assess the relationships between mitochondrial dysfunction parameters and tissue damage, correlation analysis was performed separately within each genetic background using Spearman's rank correlation coefficient (r_s). The strength of correlations was interpreted using the Chaddock scale thresholds [19].

3.4.1 Skeletal Muscle

In skeletal muscle, strong correlations were identified in both genetic backgrounds (Table 4). In the C57BL/10-based group (C57BL/10 + *mdx*), mitochondrial calcium overload positively correlated with tissue calcification (r_s = 0.85), fibrosis (r_s = 0.83), and inflammatory foci (r_s = 0.77), and negatively correlated with calcium retention capacity (CRC; r_s = –0.81). CRC negatively correlated with inflammation (r_s = –0.89), and calcification (r_s = –0.88). RCR negatively correlated with calcification (r_s = –0.82), inflammation (r_s = –0.71), and 4-HNE (r_s = –0.86). Calcification level positively correlated with inflammation (r_s = 0.80) and calpain activity (r_s = 0.87). Inflammatory foci positively correlated with 4-HNE (r_s = 0.81) and calpain activity (r_s = 0.77).

In the DBA/2-based group (DBA/2 + D2.DMD), the correlation pattern was generally similar, with some differences. Mitochondrial calcium overload positively correlated with calcification (r_s = 0.78), inflammation (r_s = 0.73), and 4-HNE (r_s = 0.95), and negatively correlated with CRC (r_s = –0.68) and RCR (r_s = –0.81). CRC negatively correlated with calcification (r_s = –0.78), fibrosis (r_s = –0.80), inflammation (r_s = –0.94), 4-HNE (r_s = –0.71), and calpain activity (r_s = –0.76). RCR demonstrated strong negative correlations with calcification (r_s = –0.90), inflammation (r_s = –0.80), 4-HNE (r_s = –0.71), and calpain activity (r_s = –0.88). Of particular note was the near-perfect positive correlation between tissue calcification and calpain activity (r_s = 1.00, $p < 0.001$), as well as strong correlations of inflammatory foci with 4-HNE (r_s = 0.86) and calpain activity (r_s = 0.87).

3.4.2 Heart

In the heart, correlation analysis revealed substantial differences between the two genetic backgrounds (Table 5). In the C57BL/10-based group, mitochondrial CRC positively correlated with RCR (r_s = 0.81), calcification (r_s = 0.66), and 4-HNE (r_s = 0.98). RCR positively correlated with calcification (r_s = 0.83), fibrosis (r_s = 0.79), and 4-HNE (r_s = 0.76). Calcification positively correlated with fibrosis (r_s = 0.88). Mitochondrial calcium overload showed a strong positive correlation with calpain activity (r_s = 0.73).

In the DBA/2-based group, the direction of several correlations reversed. Calcium overload positively correlated with calcification (r_s = 0.88) and 4-HNE (r_s = 0.83). CRC demonstrated strong negative correlations with RCR (r_s = –0.84), calcification (r_s = –0.80), and 4-HNE (r_s = –0.79). Calcification showed a near-perfect positive correlation with 4-HNE (r_s = 0.98), while fibrosis positively correlated with 4-HNE (r_s = 0.86). These findings indicate that cardiac mitochondrial dysfunction in the severe D2.DMD model differs qualitatively from that in the mild *mdx* model, likely reflecting a more profound uncoupling of calcium homeostasis and oxidative stress.

3.4.3 Liver

In the liver, the differences between the two genetic backgrounds were particularly pronounced (Table 6). In the C57BL/10-based group, only one significant correla-

Table 4. Correlation matrices for skeletal muscle parameters.

Parameter	Mitochondrial Ca^{2+} overload	Mitochondrial CRC	Mitochondrial RCR	Tissue calcification	Tissue fibrosis	Inflammatory foci	4-HNE level	Calpain activity
C57BL/10-based group (C57BL/10 + *mdx*)								
Mitochondrial Ca^{2+} overload	1.00	–0.81 ($p = 0.005$)	–0.61 ($p = 0.060$)	0.85 ($p = 0.004$)	0.83 ($p = 0.005$)	0.77 ($p = 0.016$)	0.74 ($p = 0.037$)	0.83 ($p = 0.003$)
Mitochondrial CRC	–0.81 ($p = 0.005$)	1.00	0.75 ($p = 0.013$)	–0.88 ($p = 0.002$)	–0.67 ($p = 0.050$)	–0.89 ($p = 0.001$)	–0.74 ($p = 0.037$)	–0.78 ($p = 0.008$)
Mitochondrial RCR	–0.61 ($p = 0.060$)	0.75 ($p = 0.013$)	1.00	–0.82 ($p = 0.007$)	–0.62 ($p = 0.077$)	–0.71 ($p = 0.031$)	–0.86 ($p = 0.006$)	–0.76 ($p = 0.011$)
Tissue calcification	0.85 ($p = 0.004$)	–0.88 ($p = 0.002$)	–0.82 ($p = 0.007$)	1.00	0.68 ($p = 0.042$)	0.80 ($p = 0.010$)	0.76 ($p = 0.028$)	0.87 ($p = 0.002$)
Tissue fibrosis	0.83 ($p = 0.005$)	–0.67 ($p = 0.050$)	–0.62 ($p = 0.077$)	0.68 ($p = 0.042$)	1.00	0.77 ($p = 0.016$)	0.69 ($p = 0.058$)	0.65 ($p = 0.058$)
Inflammatory foci	0.77 ($p = 0.016$)	–0.89 ($p = 0.001$)	–0.71 ($p = 0.031$)	0.80 ($p = 0.010$)	0.77 ($p = 0.016$)	1.00	0.81 ($p = 0.014$)	0.77 ($p = 0.016$)
4-HNE level	0.74 ($p = 0.037$)	–0.74 ($p = 0.037$)	–0.86 ($p = 0.006$)	0.76 ($p = 0.028$)	0.69 ($p = 0.058$)	0.81 ($p = 0.014$)	1.00	0.76 ($p = 0.028$)
Calpain activity	0.83 ($p = 0.003$)	–0.78 ($p = 0.008$)	–0.76 ($p = 0.011$)	0.87 ($p = 0.002$)	0.65 ($p = 0.058$)	0.77 ($p = 0.016$)	0.76 ($p = 0.028$)	1.00
DBA/2-based group (DBA/2 + D2.DMD)								
Mitochondrial Ca^{2+} overload	1.00	–0.68 ($p = 0.029$)	–0.81 ($p = 0.005$)	0.78 ($p = 0.013$)	0.58 ($p = 0.099$)	0.73 ($p = 0.025$)	0.95 ($p < 0.001$)	0.72 ($p = 0.019$)
Mitochondrial CRC	–0.68 ($p = 0.029$)	1.00	0.70 ($p = 0.025$)	–0.78 ($p = 0.013$)	–0.80 ($p = 0.010$)	–0.94 ($p < 0.001$)	–0.71 ($p = 0.047$)	–0.76 ($p = 0.011$)
Mitochondrial RCR	–0.81 ($p = 0.005$)	0.70 ($p = 0.025$)	1.00	–0.90 ($p < 0.001$)	–0.65 ($p = 0.058$)	–0.80 ($p = 0.010$)	–0.71 ($p = 0.047$)	–0.88 ($p = 0.001$)
Tissue calcification	0.78 ($p = 0.013$)	–0.78 ($p = 0.013$)	–0.90 ($p < 0.001$)	1.00	0.62 ($p = 0.077$)	0.87 ($p = 0.002$)	0.74 ($p = 0.037$)	1.00 ($p < 0.001$)
Tissue fibrosis	0.58 ($p = 0.099$)	–0.80 ($p = 0.010$)	–0.65 ($p = 0.058$)	0.62 ($p = 0.077$)	1.00	0.73 ($p = 0.025$)	0.60 ($p = 0.119$)	0.62 ($p = 0.077$)
Inflammatory foci	0.73 ($p = 0.025$)	–0.94 ($p < 0.001$)	–0.80 ($p = 0.010$)	0.87 ($p = 0.002$)	0.73 ($p = 0.025$)	1.00	0.86 ($p = 0.006$)	0.87 ($p = 0.002$)
4-HNE level	0.95 ($p < 0.001$)	–0.71 ($p = 0.047$)	–0.71 ($p = 0.047$)	0.74 ($p = 0.037$)	0.60 ($p = 0.119$)	0.86 ($p = 0.006$)	1.00	0.74 ($p = 0.037$)
Calpain activity	0.72 ($p = 0.019$)	–0.76 ($p = 0.011$)	–0.88 ($p = 0.001$)	1.00	0.62 ($p = 0.077$)	0.87 ($p = 0.002$)	0.74 ($p = 0.037$)	1.00

Spearman's rank correlation coefficients (r_s) and exact *p*-values between mitochondrial function parameters (calcium overload, CRC, RCR) and histopathological features (calcification, fibrosis, inflammation) as well as markers of oxidative stress (4-HNE) and calcium-dependent proteolysis (calpain) in skeletal muscle. Colour intensity reflects the magnitude of the correlation coefficient (r_s): the darker the shade, the stronger the correlation. Red indicates positive correlations; blue indicates negative correlations. White (uncoloured) cells indicate correlations that were not statistically significant. Strong correlations ($|r_s| > 0.7$) are shown in colour.

Table 5. Correlation matrix for cardiac parameters.

Parameter	Mitochondrial Ca^{2+} overload	Mitochondrial CRC	Mitochondrial RCR	Tissue calcification	Tissue fibrosis	4-HNE level	Calpain activity
C57BL/10-based group (C57BL/10 + *mdx*)							
Mitochondrial Ca^{2+} overload	1.00	0.01 ($p = 0.987$)	–0.24 ($p = 0.570$)	0.26 ($p = 0.461$)	0.17 ($p = 0.668$)	–0.05 ($p = 0.911$)	0.73 ($p = 0.017$)
Mitochondrial CRC	0.01 ($p = 0.987$)	1.00	0.81 ($p = 0.015$)	0.66 ($p = 0.039$)	0.55 ($p = 0.125$)	0.98 ($p < 0.001$)	0.60 ($p = 0.069$)
Mitochondrial RCR	–0.24 ($p = 0.570$)	0.81 ($p = 0.015$)	1.00	0.83 ($p = 0.011$)	0.79 ($p = 0.021$)	0.76 ($p = 0.028$)	0.43 ($p = 0.289$)
Tissue calcification	0.26 ($p = 0.461$)	0.66 ($p = 0.039$)	0.83 ($p = 0.011$)	1.00	0.88 ($p = 0.002$)	0.71 ($p = 0.050$)	0.61 ($p = 0.062$)
Tissue fibrosis	0.17 ($p = 0.668$)	0.55 ($p = 0.125$)	0.79 ($p = 0.021$)	0.88 ($p = 0.002$)	1.00	0.62 ($p = 0.102$)	0.42 ($p = 0.265$)
4-HNE level	–0.05 ($p = 0.911$)	0.98 ($p < 0.001$)	0.76 ($p = 0.028$)	0.71 ($p = 0.050$)	0.62 ($p = 0.102$)	1.00	0.69 ($p = 0.058$)
Calpain activity	0.73 ($p = 0.017$)	0.60 ($p = 0.069$)	0.43 ($p = 0.289$)	0.61 ($p = 0.062$)	0.42 ($p = 0.265$)	0.69 ($p = 0.058$)	1.00
DBA/2-based group (DBA/2 + D2.DMD)							
Mitochondrial Ca^{2+} overload	1.00	–0.62 ($p = 0.054$)	0.40 ($p = 0.333$)	0.88 ($p = 0.001$)	0.62 ($p = 0.077$)	0.83 ($p = 0.010$)	0.36 ($p = 0.310$)
Mitochondrial CRC	–0.62 ($p = 0.054$)	1.00	–0.84 ($p = 0.009$)	–0.80 ($p = 0.005$)	–0.58 ($p = 0.099$)	–0.79 ($p = 0.0208$)	0.13 ($p = 0.726$)
Mitochondrial RCR	0.40 ($p = 0.333$)	–0.84 ($p = 0.009$)	1.00	0.59 ($p = 0.124$)	0.35 ($p = 0.399$)	0.60 ($p = 0.117$)	–0.65 ($p = 0.083$)
Tissue calcification	0.88 ($p = 0.001$)	–0.80 ($p = 0.005$)	0.59 ($p = 0.124$)	1.00	0.56 ($p = 0.117$)	0.98 ($p < 0.001$)	0.26 ($p = 0.461$)
Tissue fibrosis	0.62 ($p = 0.077$)	–0.58 ($p = 0.099$)	0.35 ($p = 0.399$)	0.56 ($p = 0.117$)	1.00	0.86 ($p = 0.007$)	0.17 ($p = 0.668$)
4-HNE level	0.83 ($p = 0.010$)	–0.79 ($p = 0.0208$)	0.60 ($p = 0.117$)	0.98 ($p < 0.001$)	0.86 ($p = 0.007$)	1.00	0.05 ($p = 0.911$)
Calpain activity	0.36 ($p = 0.310$)	0.13 ($p = 0.726$)	–0.65 ($p = 0.083$)	0.26 ($p = 0.461$)	0.17 ($p = 0.668$)	0.05 ($p = 0.911$)	1.00

Spearman's rank correlation coefficients (r_s) and exact p-values between mitochondrial function parameters (calcium overload, CRC, RCR) and histopathological features (calcification, fibrosis) as well as markers of oxidative stress (4-HNE) and calcium-dependent proteolysis (calpain) in the heart. Colour intensity reflects the magnitude of the correlation coefficient (r_s): the darker the shade, the stronger the correlation. Red indicates positive correlations; blue indicates negative correlations. White (uncoloured) cells indicate correlations that were not statistically significant.

tion was found: CRC negatively correlated with fibrosis (r_s = –0.74, $p < 0.05$). No other significant associations were detected, suggesting that in the mild *mdx* model, liver mitochondrial dysfunction is weakly linked to tissue pathology.

In the DBA/2-based group, by contrast, numerous strong correlations were revealed. CRC demonstrated a near-perfect positive correlation with RCR (r_s = 0.96, $p <$ 0.001), as well as negative correlations with fibrosis (r_s = –0.76), ballooning degeneration (r_s = –0.82), and 4-HNE (r_s = –0.76). RCR negatively correlated with fibrosis (r_s = –0.81) and 4-HNE (r_s = –0.74). Calcium overload positively correlated with 4-HNE (r_s = 0.81). Ballooning degeneration positively correlated with 4-HNE (r_s = 0.79) and calpain activity (r_s = 0.86). These findings indicate that in the severe D2.DMD model, hepatic mitochondrial dysfunction is tightly linked to tissue damage, oxidative stress, and calcium-dependent proteolysis, whereas in the mild *mdx* model, the liver remains largely unaffected at the functional level.

4. Discussion

This study provides a comparative analysis of mitochondrial dysfunction, oxidative stress and calcium-dependent proteolysis, as well as histopathological and ultrastructural changes in skeletal muscle, heart, and liver between two mouse models of DMD: the classical *mdx* line on the C57BL/10 genetic background with a mild phenotype and the severe D2.DMDdel8-34 line on the DBA/2 genetic background. Our data demonstrate that the severity of mitochondrial dysfunction correlates with the extent of tissue damage and exhibits tissue-specific patterns, with the D2.DMDdel8-34 line recapitulating a more severe pathology that more closely mirrors the clinical picture of human DMD.

The D2.DMDdel8-34 line was generated by transferring the DMDdel8-34 mutation, originally identified in a Russian patient with severe DMD [20], onto the DBA/2 genetic background, which is associated with a more severe course of dystrophinopathy in *mdx*-based models [5]. Thus, D2.DMDdel8-34 represents an analogue of the D2-*mdx* line, differing only in the primary mutation in the *Dmd* gene, and, like D2-*mdx*, exhibits a more severe phenotype compared with *mdx* on the C57BL/10 genetic background [5,7,8]. The *mdx* and D2.DMDdel8-34 lines differ in both the *Dmd* mutation and the genetic background. The severe phenotype of D2.DMDdel8-34 is consistent with the known exacerbating effect of the DBA/2 background on dystrophic pathology [5], suggesting that the genetic background may be an important contributing factor to disease severity, although the specific mutation may also play a role. However, the precise contribution of background modifiers to the mitochondrial phenotype remains to be fully established.

Validation of the models confirmed that the D2.DMDdel8-34 line is characterized by a significantly more severe phenotype compared with *mdx* across all organs examined. Functional tests revealed a more pronounced reduction in grip strength and endurance in D2.DMD compared with *mdx*, consistent with published data on the more severe course of dystrophinopathy on the DBA/2 genetic background [4,5,7,8]. Histological analysis of skeletal muscle showed that in D2.DMD, the extent of fibrosis and calcification, as well as the number of inflammatory infiltrates, significantly exceeded those in *mdx*, whereas the proportion of centrally nucleated fibers was significantly lower, reflecting the diminished regenerative capacity of muscle fibers on the DBA/2 background [4,5]. These findings are in agreement with the work of Tinklenberg and colleagues [8], who demonstrated that D2-*mdx* exhibits more severe muscle pathology compared with B10-*mdx*. An interesting observation was the reduced serum CK levels in D2.DMD compared with *mdx*, despite the more severe histological changes. Notably, the relative increase in CK over the respective control was similar in both dystrophic lines (~2-fold), while the absolute values were lower in the DBA/2-based groups. This suggests that the lower CK levels in D2.DMD may partly reflect the lower baseline CK levels characteristic of the DBA/2 genetic background. However, the marked atrophy and extensive fibrosis typical of the severe D2.DMD phenotype likely also contribute by depleting the intramuscular CK pool and limiting enzyme release into the bloodstream. Thus, interpretation of serum CK levels in severe DMD models requires caution and consideration of both genetic background effects and the degree of muscle atrophy and fibrosis. In the heart and liver, histopathological changes were also more pronounced in the D2.DMD line. The myocardium showed markedly elevated levels of fibrosis and calcification, consistent with data on earlier cardiac involvement in D2-*mdx* [4,5]. Pronounced hepatic changes were observed in D2.DMD, including marked ballooning degeneration, Councilman bodies (apoptosis markers), and lymphohistiocytic infiltration, indicating involvement of this organ in the pathological process associated with the severe DMD phenotype.

An important consideration is the interpretation of the lower proportion of CNF in D2.DMD compared to *mdx*. CNF reflects the cumulative history of successful regeneration rather than the severity of current damage. In *mdx* mice, the relatively preserved regenerative capacity leads to repeated cycles of degeneration and regeneration, resulting in a high proportion of CNF. In contrast, the DBA/2 genetic background carries a mutation in *Anxa6*, which impairs regenerative myogenesis [17,21]. Consequently, in D2.DMD mice, damaged muscle fibers are not effectively replaced, leading to their progressive replacement by fibrotic and calcified tissue. This is reflected in the significantly higher levels of fibrosis, inflammation, and calcification in D2.DMD compared to *mdx*. Thus, the lower CNF in D2.DMD does not indicate milder damage but rather re-

Table 6. Correlation matrix for liver parameters.

Parameter	Mitochondrial Ca^{2+} overload	Mitochondrial CRC	Mitochondrial RCR	Tissue fibrosis	Ballooning degeneration	4-HNE level	Calpain activity
C57BL/10-based group (C57BL/10 + *mdx*)							
Mitochondrial Ca^{2+} overload	1.00	0.04 ($p = 0.907$)	0.01 ($p = 0.973$)	0.00 ($p = 1.000$)	0.14 ($p = 0.760$)	0.14 ($p = 0.736$)	–0.52 ($p = 0.183$)
Mitochondrial CRC	0.04 ($p = 0.907$)	1.00	0.21 ($p = 0.555$)	–0.74 ($p = 0.037$)	–0.46 ($p = 0.294$)	0.62 ($p = 0.102$)	–0.05 ($p = 0.911$)
Mitochondrial RCR	0.01 ($p = 0.973$)	0.21 ($p = 0.555$)	1.00	0.60 ($p = 0.117$)	0.65 ($p = 0.115$)	–0.14 ($p = 0.734$)	0.29 ($p = 0.490$)
Tissue fibrosis	0.00 ($p = 1.000$)	–0.74 ($p = 0.037$)	0.60 ($p = 0.117$)	1.00	0.64 ($p = 0.119$)	–0.36 ($p = 0.385$)	0.17 ($p = 0.693$)
Ballooning degeneration	0.14 ($p = 0.760$)	–0.46 ($p = 0.294$)	0.65 ($p = 0.115$)	0.64 ($p = 0.119$)	1.00	–0.43 ($p = 0.337$)	0.25 ($p = 0.589$)
4-HNE level	0.14 ($p = 0.736$)	0.62 ($p = 0.102$)	–0.14 ($p = 0.734$)	–0.36 ($p = 0.385$)	–0.43 ($p = 0.337$)	1.00	0.14 ($p = 0.736$)
Calpain activity	–0.52 ($p = 0.183$)	–0.05 ($p = 0.911$)	0.29 ($p = 0.490$)	0.17 ($p = 0.693$)	0.25 ($p = 0.589$)	0.14 ($p = 0.736$)	1.00
DBA/2-based group (DBA/2 + D2.DMD)							
Mitochondrial Ca^{2+} overload	1.00	–0.65 ($p = 0.042$)	–0.62 ($p = 0.054$)	0.17 ($p = 0.693$)	0.71 ($p = 0.071$)	0.81 ($p = 0.015$)	0.55 ($p = 0.160$)
Mitochondrial CRC	–0.65 ($p = 0.042$)	1.00	0.96 ($p < 0.001$)	–0.76 ($p = 0.028$)	–0.82 ($p = 0.023$)	–0.76 ($p = 0.028$)	–0.55 ($p = 0.160$)
Mitochondrial RCR	–0.62 ($p = 0.054$)	0.96 ($p < 0.001$)	1.00	–0.81 ($p = 0.015$)	–0.75 ($p = 0.052$)	–0.74 ($p = 0.037$)	–0.52 ($p = 0.183$)
Tissue fibrosis	0.17 ($p = 0.693$)	–0.76 ($p = 0.028$)	–0.81 ($p = 0.015$)	1.00	0.54 ($p = 0.215$)	0.33 ($p = 0.420$)	0.48 ($p = 0.233$)
Ballooning degeneration	0.71 ($p = 0.071$)	–0.82 ($p = 0.023$)	–0.75 ($p = 0.052$)	0.54 ($p = 0.215$)	1.00	0.79 ($p = 0.036$)	0.86 ($p = 0.014$)
4-HNE level	0.81 ($p = 0.015$)	–0.76 ($p = 0.028$)	–0.74 ($p = 0.037$)	0.33 ($p = 0.420$)	0.79 ($p = 0.036$)	1.00	0.50 ($p = 0.207$)
Calpain activity	0.55 ($p = 0.160$)	–0.55 ($p = 0.160$)	–0.52 ($p = 0.183$)	0.48 ($p = 0.233$)	0.86 ($p = 0.014$)	0.50 ($p = 0.207$)	1.00

Spearman's rank correlation coefficients (r_s) and exact *p*-values between mitochondrial function parameters (calcium overload, CRC, RCR) and histopathological features (fibrosis, ballooning degeneration) as well as markers of oxidative stress (4-HNE) and calcium-dependent proteolysis (calpain) in the liver. Colour intensity reflects the magnitude of the correlation coefficient (r_s): the darker the shade, the stronger the correlation. Red indicates positive correlations; blue indicates negative correlations. White (uncoloured) cells indicate correlations that were not statistically significant.

flects failed regeneration. This distinction is critical when comparing the severity of muscle pathology between the two models and when interpreting histomorphometric data in preclinical studies.

The key finding of this work is the demonstration that mitochondrial dysfunction in the D2.DMDdel8-34 line is significantly more pronounced across all three organs examined compared with the *mdx* line. In skeletal muscle, D2.DMD showed a reduction in state 3 respiration and RCR, indicating a more severe impairment of oxidative phosphorylation coupling. Recently, Tinklenberg and colleagues [8] showed that D2-*mdx* exhibits almost complete absence of mitochondrial respiration and undetectable ATP levels in skeletal muscle compared with B10-*mdx*. Our data confirm and extend these observations, demonstrating that similar, although less dramatic, alterations are present in the heart and liver. In the heart, D2.DMD exhibited reduced state 3 respiration and RCR compared with DBA/2, whereas *mdx* showed a tendency toward increased values of these parameters. In the liver, RCR was reduced in D2.DMD to levels comparable to C57BL/10 and *mdx*, whereas in DBA/2 this parameter was elevated. Notably, the DBA/2 genetic background is characterized by higher basal mitochondrial respiratory activity, which may be related to differences in respiratory chain organization and supercomplex assembly [22]. However, the development of dystrophinopathy on this background leads to a more profound suppression of oxidative phosphorylation than in *mdx*. Notably, respiratory alterations in the heart and liver of *mdx* were less pronounced or absent, consistent with the later involvement of these organs in the pathological process in the classical DMD model [4,5].

An important finding of this study is the extent of mitochondrial dysfunction in the liver of D2.DMD mice, a non-contractile tissue not exposed to the mechanical stress that drives muscle pathology. Notably, Tinklenberg and colleagues [8] previously demonstrated that known genetic modifiers present on the DBA/2 background, such as *Ltbp4* and *Anxa6*, do not account for the severe mitochondrial deficiency observed in D2-*mdx* mice. This suggests that the profound mitochondrial impairment in D2.DMD is not a direct consequence of these modifier alleles. Given that we observed a similar, though less pronounced, increased basal respiratory activity in mitochondria from the liver and heart of healthy DBA/2 mice compared to C57BL/10, we hypothesize that the DBA/2 genetic background may confer a tissue-wide vulnerability of mitochondria to stress. The inherently higher mitochondrial respiratory capacity of DBA/2 mice may be coupled with elevated baseline oxidative stress or reduced mitochondrial quality control, making mitochondria in all organs, including the liver, more susceptible to the secondary insults triggered by dystrophin deficiency. Thus, while the primary driver of muscle pathology is dystrophin deficiency, the systemic metabolic milieu of the DBA/2 background may amplify mitochondrial dysfunction in a tissue-independent manner, explaining why the D2.DMD model recapitulates a more severe phenotype even in non-mechanical organs such as the liver. This interpretation is supported by the stratified correlation analysis, which revealed numerous strong associations between mitochondrial dysfunction and tissue pathology in the liver of the DBA/2-based group, whereas in the C57BL/10-based group, such associations were strong in skeletal muscle but largely absent in the heart and liver. It is tempting to speculate that early cardiac dysfunction in D2.DMD, unlike the mild cardiac phenotype in *mdx*, may contribute to hepatic pathology through hemodynamic disturbances, such as venous congestion, as supported by the pronounced sinusoidal congestion observed in D2.DMD livers (**Supplementary Fig. 6**). This could explain why hepatic involvement is more severe in the D2.DMD model, although further studies are required to establish causal relationships.

Mitochondrial calcium homeostasis emerged as a key differentiating factor between the two models. In skeletal muscle of D2.DMD, we observed significantly higher calcium overload and, consequently, a more profound reduction in CRC compared with *mdx*. Correlation analysis revealed strong associations between calcium overload and histopathological changes (fibrosis, calcification, inflammation) in skeletal muscle, suggesting that mitochondrial calcium overload may play an important role in the pathogenesis of tissue damage. In the heart, correlation patterns differed markedly between the two genetic backgrounds. In the C57BL/10-based group, the positive correlations between CRC, RCR, and histopathological markers suggest a compensatory phase of mitochondrial adaptation, where increased mitochondrial function is associated with greater tissue damage, likely reflecting an early stress response [23,24]. Consistent with this, *mdx* hearts exhibited increased CRC relative to both C57BL/10 and DBA/2, supporting the idea of a compensatory response. In contrast, in the DBA/2-based group, the reversal of these correlations is consistent with a decompensated state, where impaired mitochondrial calcium handling and respiratory dysfunction are associated with tissue injury. This qualitative shift in correlation patterns underscores the progressive nature of mitochondrial failure in the severe D2.DMD model. These findings suggest that the DBA/2 genetic background may contribute to the development of decompensation in the dystrophic heart. However, further studies are required to confirm this hypothesis. A strikingly different pattern was observed in the liver, where, unlike skeletal muscle and heart, the reduction in CRC was more strongly associated with impaired respiratory function and oxidative stress than with calcium overload, as supported by the strong positive correlation between CRC and RCR (r_s = 0.96) and the negative correlations of CRC with 4-HNE (r_s = –0.76) and ballooning degeneration (r_s = –0.82) in the DBA/2-based group. Notably, calcium overload in liver mitochondria itself showed a strong positive correla-

tion with 4-HNE (r_s = 0.81), suggesting that calcium overload and oxidative stress are closely associated in the liver, and that the link between calcium dysregulation and tissue damage in this organ may be primarily mediated through oxidative stress pathways rather than through direct mitochondrial calcium-induced injury. Stratified correlation analysis showed that in the C57BL/10-based group, no significant associations between CRC and RCR were found in the liver, whereas in the DBA/2-based group a near-perfect positive correlation was revealed between these parameters (r_s = 0.96, $p < 0.001$), suggesting an association between reduced calcium retention capacity and impaired respiratory function. Furthermore, the reduction in hepatic CRC in D2.DMD was associated with both calcium overload and, to a much greater extent, respiratory impairment. Strong negative correlations of CRC with fibrosis, ballooning degeneration, and 4-HNE indicate that reduced mitochondrial resistance to mPTP induction is associated with histopathological changes in the liver in the severe phenotype. However, these findings are based on cross-sectional correlations and do not establish causality, the possibility that a third factor contributes to both mitochondrial dysfunction and liver pathology cannot be excluded. Further studies are needed to determine whether the tissue-specific mechanisms of mitochondrial dysfunction identified here can be targeted therapeutically.

Analysis of oxidative stress markers and calcium-dependent proteolysis revealed pronounced tissue-specific differences. In skeletal muscle, 4-HNE levels and calpain activity were highest in D2.DMD, correlating with the severity of histopathological changes. Calpain activity in skeletal muscle of D2.DMD was elevated 7-fold compared with control, significantly exceeding the activation level observed in *mdx*. This is consistent with the findings of Cleverdon and colleagues [25], who showed that calpain activity in D2-*mdx* is significantly higher than in C57-*mdx*. In the heart and liver, calpain activity did not differ between dystrophin-deficient mice and their respective controls, indicating tissue-specificity of calpain-mediated injury mechanisms. The elevation of calpain activity is restricted to skeletal muscle in dystrophin deficiency, since mechanical stability of the sarcolemma and calcium homeostasis are most severely compromised in this tissue. In skeletal muscle, the absence of dystrophin renders fibers more susceptible to membrane microdamage, chronic Ca^{2+} influx, and dysregulated calcium handling, which may directly activate calpains and exacerbates fiber destruction [26,27]. In the *mdx* heart, cardiomyocytes may also exhibit Ca^{2+} dysregulation, but this often manifests later than in skeletal muscle [28]. Furthermore, cardiac tissue differs in dystrophin-associated complex composition and has higher calpastatin levels, which may limit net calpain activity despite the presence of triggers [29,30]. The liver, by contrast, does not bear such mechanical load and is not considered a primary site of Ca^{2+}-dependent damage in DMD.

Ultrastructural analysis not only confirmed the functional impairments but also revealed qualitative and quantitative differences in mitochondrial dynamics between tissues and models. In skeletal muscle of D2.DMD, the most severe destructive changes were observed: myofibrillar disorganization, Z-disk disruption, a marked reduction in mitochondrial number and size against a background of pronounced accumulation of mitophagosomes. This suggests a predominance of elimination of damaged organelles over their biogenesis, leading to depletion of the mitochondrial pool and consistent with the low respiratory activity and calcium retention capacity in the severe model. In *mdx*, these changes were less pronounced and mosaic in nature, which may reflect a more balanced ratio between degradation and restoration of organelles. In the heart, a different picture emerged: mitochondrial number in DBA/2 and D2.DMD was higher than in C57BL/10, although it did not differ from *mdx*, while the number of mitophagosomes maximally exceeded the levels in DBA/2 and *mdx*. This may indicate compensatory biogenesis that partially counteracts enhanced mitophagy, however, the abundance of pathological forms (megamitochondria, septated mitochondria, organelles with micromitophagosomes) suggests the inefficiency of this process. The divergent changes in mitochondrial dynamics in skeletal muscle and heart reflect tissue-specific adaptive responses to dystrophin deficiency and may explain why heart failure in DMD develops through a different scenario than skeletal muscle degeneration. These data are consistent with the work of Hayes and colleagues [31], who showed heterogeneous zones of myocardial disorganization and compensatory mitochondrial proliferation in D2-*mdx*.

However, it should be noted that static TEM measurements alone cannot distinguish between increased mitophagic flux and impaired clearance, nor can they directly demonstrate mitochondrial biogenesis. Therefore, these interpretations should be considered as possible explanations rather than established mechanisms.

Thus, stratified correlation analysis revealed that the nature and strength of associations between mitochondrial dysfunction and tissue pathology largely depend on the genetic background. In skeletal muscle, these associations were strong in both backgrounds, whereas in the heart and liver, fundamental differences were observed between the C57BL/10- and DBA/2-based groups. These data support the concept that mitochondrial dysfunction is a key secondary mechanism in DMD pathogenesis. However, its manifestations and interconnections with tissue damage are substantially modulated by the genetic context. The D2.DMD model is valuable for studying systemic mitochondrial pathology. However, its specific features, including pronounced calcification and impaired skeletal muscle regeneration, should be carefully considered when designing preclinical studies.

5. Limitations

This study has several limitations that should be considered when interpreting the results. First, the two DMD models used in this study (*mdx* and D2.DMD) differ in both the *Dmd* mutation and the genetic background, which does not allow us to fully separate mutation-specific effects from background-dependent modifiers. Second, the study was performed at a single time point (8 weeks of age), which limits our ability to draw conclusions about the temporal sequence of mitochondrial and histopathological changes. Third, the D2.DMD model exhibits certain features that do not fully recapitulate human DMD pathology, including pronounced tissue calcification. In addition, the lower proportion of centrally nucleated fibers in D2.DMD reflects impaired regenerative capacity on the DBA/2 background rather than a milder degenerative process, which should be considered when interpreting histomorphometric data. These differences should be taken into account when extrapolating findings to the human disease. Fourth, transmission electron microscopy was performed only in skeletal muscle and heart, but not in the liver, and the number of animals used for TEM analysis was limited (n = 3 per group). Moreover, the interpretation of TEM data is limited by the static nature of the analysis, which cannot distinguish between increased mitophagic flux and impaired clearance, or directly demonstrate mitochondrial biogenesis. Finally, the study did not include functional cardiac measurements (echocardiography), which would have provided a more comprehensive assessment of cardiac involvement. The Knodell HAI score, while useful for standardized assessment, was not specifically validated for DMD models. Despite these limitations, the study provides a systematic multi-organ comparison of mitochondrial dysfunction in mild and severe DMD models and identifies tissue-specific patterns that may inform future preclinical research.

6. Conclusions

The present study demonstrates that the severe D2.DMDdel8-34 model on the DBA/2 genetic background exhibits profound mitochondrial dysfunction across all three organs examined (skeletal muscle, heart, and liver), manifesting as impaired oxidative phosphorylation and disturbed calcium homeostasis. The identified organ-specificity of pathological mechanisms substantiates the need for a differentiated approach to the development of mitochondria-targeted therapeutic strategies.

Importantly, stratified correlation analysis revealed that the associations between mitochondrial dysfunction and tissue pathology are highly dependent on the genetic background. In the D2.DMD model, mitochondrial dysfunction was associated with tissue damage and oxidative stress in all three organs. However, the D2.DMD model also exhibits specific features that distinguish it from human DMD, including pronounced tissue calcification and impaired skeletal muscle regeneration (reflected in lower CNF and higher fibrosis compared to *mdx*). These limitations should be taken into account when using this model for preclinical research. Further studies should focus on assessing the long-term consequences of mitochondrial dysfunction and developing combined approaches that take into account the organ-specificity of pathological processes in DMD.

Abbreviations

CRC, calcium retention capacity; DMD, Duchenne muscular dystrophy; HAI, histological activity index; 4-HNE, 4-hydroxynonenal; mPTP, mitochondrial permeability transition pore; RCR, respiratory control ratio; CK, creatine kinase; CNF, centrally nucleated fibers; H&E, hematoxylin and eosin.

Availability of Data and Materials

The datasets used and analyzed during the current study are available from the corresponding author upon reasonable request.

Author Contributions

MVD designed the research study. MVD, AES, ADI, GPD, ASU, AAS, IBM, SOR, ENK, KNB and TVE performed the research. MVD, AES, GPD, IBM and KNB analyzed the data. MVD wrote the manuscript. All authors contributed to editorial changes in the manuscript. All authors read and approved the final manuscript. All authors have participated sufficiently in the work and agreed to be accountable for all aspects of the work.

Ethics Approval and Consent to Participate

The study with mice was in line with the European Convention for the Protection of Vertebrate Animals Used for Experimental and Other Scientific Purposes (Strasbourg, 1986). The research protocol was approved by the Mari State University Ethics Committee (protocol No. 01/2024 of 11.11.2024). The study was carried out in accordance with the ARRIVE guidelines.

Acknowledgment

Not applicable.

Funding

This work was supported by grant from the Russian Science Foundation (23-75-10006, https://rscf.ru/project/23-75-10006/).

Conflicts of Interest

The authors declare no conflicts of interest. Given his role as the Guest Editor, Mikhail V. Dubinin had no involvement in the peer review of this article and has no ac-

cess to information regarding its peer review. Full responsibility for the editorial process for this article was delegated to Graham Pawelec.

Declaration of AI and AI-Assisted Technologies in the Writing Process

During the preparation of this work, the authors used DeepSeek in order to check spelling and grammar. After using this tool, the authors reviewed and edited the content as needed and take full responsibility for the content of the publication.

Supplementary Material

Supplementary material associated with this article can be found, in the online version, at https://doi.org/10.31083/FBL56498.

References

[1] Epis R, Rovetta G, Ferrari G, Bonfanti C, Careccia G, Messina G. Downstream Pathways of Dystrophin Deficiency in Duchenne Muscular Dystrophy: Implications for Muscle Degeneration and Regeneration. Journal of Cachexia, Sarcopenia and Muscle. 2026; 17: e70333. https://doi.org/10.1002/jcsm.70333

[2] Delafenêtre A, Chapotte-Baldacci CA, Dorémus L, Massouridès E, Bernard M, Régnacq M, et al. Duchenne muscular dystrophy skeletal muscle cells derived from human induced pluripotent stem cells recapitulate various calcium dysregulation pathways. Cell Calcium. 2024; 123: 102943. https://doi.org/10.1016/j.ceca.2024.102943

[3] Dubinin MV, Belosludtsev KN. Ion Channels of the Sarcolemma and Intracellular Organelles in Duchenne Muscular Dystrophy: A Role in the Dysregulation of Ion Homeostasis and a Possible Target for Therapy. International Journal of Molecular Sciences. 2023; 24: 2229. https://doi.org/10.3390/ijms24032229

[4] Coley WD, Bogdanik L, Vila MC, Yu Q, Van Der Meulen JH, Rayavarapu S, et al. Effect of genetic background on the dystrophic phenotype in mdx mice. Human Molecular Genetics. 2016; 25: 130–145. https://doi.org/10.1093/hmg/ddv460

[5] van Putten M, Putker K, Overzier M, Adamzek WA, Pasteuning-Vuhman S, Plomp JJ, et al. Natural disease history of the D2-mdx mouse model for Duchenne muscular dystrophy. FASEB Journal: Official Publication of the Federation of American Societies for Experimental Biology. 2019; 33: 8110–8124. https://doi.org/10.1096/fj.201802488R

[6] De Luca A. Pre-clinical drug tests in the mdx mouse as a model of dystrophinopathies: an overview. Acta Myologica: Myopathies and Cardiomyopathies: Official Journal of the Mediterranean Society of Myology. 2012; 31: 40–47.

[7] Dubinin MV, Stepanova AE, Mikheeva IB, Igoshkina AD, Kraeva EN, Cherepanova AA, et al. VBIT-4 Rescues Mitochondrial Dysfunction and Reduces Skeletal Muscle Degeneration in a Severe Model of Duchenne Muscular Dystrophy. International Journal of Molecular Sciences. 2025; 26: 8845. https://doi.org/10.3390/ijms26188845

[8] Tinklenberg JA, Sutton J, Slick RA, Meng H, Haberman M, Prom MJ, et al. The D2.B10-Dmdmdx/J Mouse Model of Duchenne Muscular Dystrophy Exhibits a Severe Mitochondrial Deficiency Not Observed in the C57BL/10ScSn-Dmdmdx/J Mouse. The American Journal of Pathology. 2026; 196: 532–549. https://doi.org/10.1016/j.ajpath.2025.09.005

[9] Murphy S, Zweyer M, Henry M, Meleady P, Mundegar RR, Swandulla D, et al. Proteomic profiling of liver tissue from the mdx-4cv mouse model of Duchenne muscular dystrophy. Clinical Proteomics. 2018; 15: 34. https://doi.org/10.1186/s12014-018-9212-2

[10] van Putten M. The use of hanging wire tests to monitor muscle strength and condition over time. TREAT-NMD. 2012; 1–12.

[11] Knodell RG, Ishak KG, Black WC, Chen TS, Craig R, Kaplowitz N, et al. Formulation and application of a numerical scoring system for assessing histological activity in asymptomatic chronic active hepatitis. Hepatology (Baltimore, Md.). 1981; 1: 431–435. https://doi.org/10.1002/hep.1840010511

[12] Dubinin MV, Starinets VS, Belosludtseva NV, Mikheeva IB, Chelyadnikova YA, Igoshkina AD, et al. BKCa Activator NS1619 Improves the Structure and Function of Skeletal Muscle Mitochondria in Duchenne Dystrophy. Pharmaceutics. 2022; 14: 2336. https://doi.org/10.3390/pharmaceutics14112336

[13] Kumar A, Accorsi A, Rhee Y, Girgenrath M. Do's and don'ts in the preparation of muscle cryosections for histological analysis. Journal of Visualized Experiments: JoVE. 2015; e52793. https://doi.org/10.3791/52793

[14] Frezza C, Cipolat S, Scorrano L. Organelle isolation: functional mitochondria from mouse liver, muscle and cultured fibroblasts. Nature Protocols. 2007; 2: 287–295. https://doi.org/10.1038/nprot.2006.478

[15] CHANCE B, WILLIAMS GR. Respiratory enzymes in oxidative phosphorylation. I. Kinetics of oxygen utilization. The Journal of Biological Chemistry. 1955; 217: 383–393.

[16] Bround MJ, Havens JR, York AJ, Sargent MA, Karch J, Molkentin JD. ANT-dependent MPTP underlies necrotic myofiber death in muscular dystrophy. Science Advances. 2023; 9: eadi2767. https://doi.org/10.1126/sciadv.adi2767

[17] Rodrigues M, Echigoya Y, Maruyama R, Lim KRQ, Fukada SI, Yokota T. Impaired regenerative capacity and lower revertant fibre expansion in dystrophin-deficient mdx muscles on DBA/2 background. Scientific Reports. 2016; 6: 38371. https://doi.org/10.1038/srep38371

[18] Endlicher R, Drahota Z, Štefková K, Červinková Z, Kučera O. The Mitochondrial Permeability Transition Pore-Current Knowledge of Its Structure, Function, and Regulation, and Optimized Methods for Evaluating Its Functional State. Cells. 2023; 12: 1273. https://doi.org/10.3390/cells12091273

[19] Nikitina MA, Chernukha IM. Nonparametric statistics. Part 3. Correlation coefficients. Theory and Practice of Meat Processing. 2023; 8: 237–251. https://doi.org/10.21323/2414-438x-2023-8-3-237-251

[20] Egorova TV, Zotova ED, Reshetov DA, Polikarpova AV, Vassilieva SG, Vlodavets DV, et al. CRISPR/Cas9-generated mouse model of Duchenne muscular dystrophy recapitulating a newly identified large 430 kb deletion in the human DMD gene. Disease Models & Mechanisms. 2019; 12: dmm037655. https://doi.org/10.1242/dmm.037655

[21] Swaggart KA, Demonbreun AR, Vo AH, Swanson KE, Kim EY, Fahrenbach JP, et al. Annexin A6 modifies muscular dystrophy by mediating sarcolemmal repair. Proceedings of the National Academy of Sciences of the United States of America. 2014; 111: 6004–6009. https://doi.org/10.1073/pnas.1324242111

[22] Buck KJ, Walter NA, Denmark DL. Genetic variability of respiratory complex abundance, organization and activity in mouse brain. Genes, brain, and behavior. 2014; 13: 135–43. https://doi.org/10.1111/gbb.12101

[23] Ascah A, Khairallah M, Daussin F, Bourcier-Lucas C, Godin R, Allen BG, et al. Stress-induced opening of the permeability transition pore in the dystrophin-deficient heart is attenuated by acute treatment with sildenafil. American Journal of Physiology. Heart and Circulatory Physiology. 2011; 300: H144–H153. https://doi.org/10.1152/ajpheart.00522.2010

[24] Dubinin MV, Starinets VS, Chelyadnikova YA, Belosludtseva NV, Mikheeva IB, Penkina DK, et al. Effect of Large-Conductance Calcium-Dependent K^+ Channel Activator NS1619 on Function of Mitochondria in the Heart of Dystrophin-Deficient Mice. Biochemistry. Biokhimiia. 2023; 88: 189–201. https://doi.org/10.1134/s0006297923020037

[25] Cleverdon REG, Braun JL, Geromella MS, Whitley KC, Marko DM, Hamstra SI, et al. Sarco(endo)plasmic reticulum Ca^{2+}-ATPase function is impaired in skeletal and cardiac muscles from young DBA/2J mdx mice. iScience. 2022; 25: 104972. https://doi.org/10.1016/j.isci.2022.104972

[26] Spencer MJ, Mellgren RL. Overexpression of a calpastatin transgene in mdx muscle reduces dystrophic pathology. Human Molecular Genetics. 2002; 11: 2645–2655. https://doi.org/10.1093/hmg/11.21.2645

[27] Whitehead NP, Yeung EW, Allen DG. Muscle damage in mdx (dystrophic) mice: role of calcium and reactive oxygen species. Clinical and Experimental Pharmacology & Physiology. 2006; 33: 657–662. https://doi.org/10.1111/j.1440-1681.2006.04394.x

[28] Bremner SB, Mandrycky CJ, Leonard A, Padgett RM, Levinson AR, Rehn ES, et al. Full-length dystrophin deficiency leads to contractile and calcium transient defects in human engineered heart tissues. Journal of Tissue Engineering. 2022; 13: 20417314221119628. https://doi.org/10.1177/20417314221119628

[29] Arnold MK, Parr T, Sensky PL, Bardsley RG, Buttery PJ. Differential calpastatin expression in cardiac and skeletal muscle. Biochemical Society Transactions. 1995; 23: 454S. https://doi.org/10.1042/bst023454s

[30] Johnson EK, Zhang L, Adams ME, Phillips A, Freitas MA, Froehner SC, et al. Proteomic analysis reveals new cardiac-specific dystrophin-associated proteins. PloS one. 2012; 7: e43515. https://doi.org/10.1371/journal.pone.0043515

[31] Hayes HM, Angerosa J, Piers AT, White JD, Koleff J, Thurgood M, et al. Preserved Left Ventricular Function despite Myocardial Fibrosis and Myopathy in the Dystrophin-Deficient D2.B10-Dmd *mdx* /J Mouse. Oxidative Medicine and Cellular Longevity. 2022; 2022: 5362115. https://doi.org/10.1155/2022/5362115